Multi-material adhesive joints with thick bond-lines

Crack onset and crack deflection

Lopes Fernandes, Romina; Budzik, Michal K.; Benedictus, Rinze; Teixeira de Freitas, Sofia

DOI
10.1016/j.compstruct.2021.113687

Publication date
2021

Document Version
Final published version

Published in
Composite Structures

Composite Structures 266 (2021) 113687

Contents lists available at ScienceDirect

Composite Structures

journal homepage: www.elsevier.com/locate/compstruct

Multi-material adhesive joints with thick bond-lines: Crack onset and crack deflection

Romina Lopes Fernandes [a], Michal K. Budzik [b], Rinze Benedictus [a], Sofia Teixeira de Freitas [a,*]

[a] Structural Integrity & Composites Group, Faculty of Aerospace Engineering, Delft University of Technology, P.O. Box 5058, 2600 GB Delft, The Netherlands
[b] Group for Mechanics of Interfaces & Adhesion, Department of Engineering, Aarhus University, Inge Lehmanns Gade 10, 8000 Aarhus C, Denmark

ARTICLE INFO

Keywords:
Fracture onset
Mode I
Thick bond-line

ABSTRACT

This study investigates the fracture onset and crack deflection in multi-material adhesive joints with thick bond-lines (≈10 mm) under global mode I loading. The role of adherend-adhesive modulus-mismatch and pre-crack length are scrutinized. The parameters controlling the crack path directional stability are also discussed. Single-material (i.e. steel-steel and GFRP-GFRP) and bi-material (i.e. steel-GFRP) double-cantilever beam joints bonded with a structural epoxy adhesive are tested. The joints are modelled analytically, considering a beam on elastic-plastic foundation, to include characteristic length scales of the problem (e.g. adhesive thickness, plastic zone) and numerically using Finite Element Model. An empirical relation, in terms of geometrical and material properties of the joints, that defines the transition between non-cohesive and cohesive fracture onset is found. Above a specific pre-crack length the stress singularity at pre-crack tip rules over the stress singularity near bi-material corners, resulting in mid-adhesive thickness cohesive fracture onset. However, the cracking direction rapidly deflects out from the adhesive layer centre-line. Positive *T*-stress along the crack tip is found to be one of the factors for the unstable crack path.

1. Introduction

In shipbuilding and civil industries, demand of increased cargo transport and renovation of bridges create a set of challenges for which the use of a combination of steel and composite parts can be an attractive solution [1,2]. These parts need to be joined together. Adhesive bonding can provide structural integrity while allowing for a more smooth load transfer than bolted connections.

The use of adhesive bonding technology, in these industries, results in bonded regions characterized by adhesive layers with a thickness of up to 10 mm. Such adhesive thicknesses are imposed by manufacturing [3] and in-service constraints, and differ from other industries such as aerospace and automotive, where the manufacturing tolerances are strictly controlled, resulting in much thinner bonded regions, in general in the sub-millimetre range. On the other hand, examples of thicker bond-lines can be found in e.g. wind turbine blades, where thickness can go up to few centimeters. [4].

With such bond-line thicknesses, a weakness to be recognized, from both the scientific and applied points of view, is the stress gradient at the bi-material adhesive-adherends edges and corners, exacerbated by differences in materials properties [5–9]. Locally, peel forces arise and might result in local damage and fracture onset, in case the bonded region is subjected to external loading. The fracture mode I loading case is the most critical for an adhesive joint and, therefore, is the object of study in this paper.

Moreover, structural epoxy adhesives are often indicated, by the shipbuilding and civil engineers, to be used in the bi-material joints. Their elastic-plastic material characteristics, in addition to the aforementioned geometric length scale of the thickness of the adhesive layer, introduces a material length scale of a plastic radius [10]. When the yield strength of the adhesive is exceeded in the region near a crack tip, plastic deformation occurs in a small region, as it is restricted by the surrounding material, which remains elastic. This plastic deformation is considered as responsible for dissipation of the majority of the external loading. Control over e.g. the number, the localization and size of the plastic regions is highly desired and in principle could increase both reliability and overall performance of the joint in sustaining external loading [11].

The double-cantilever beam (DCB) specimen has been an attractive configuration for the study of crack propagation under mode I loading conditions in composites and in adhesively bonded materials due to its experimental and theoretical simplicity. The theoretical description of

* Corresponding author.
E-mail address: S.TeixeiradeFreitas@tudelft.nl (S. Teixeira de Freitas).

https://doi.org/10.1016/j.compstruct.2021.113687
Received 19 November 2020; Revised 18 January 2021; Accepted 2 February 2021
Available online 3 March 2021
0263-8223/

Nomenclature

Latin Symbols

a	crack length (mm)
a_{total}	total crack length (mm)
$a_{0\text{total}}$	initial total crack length (mm)
a_0	initially unbonded length (mm)
B	specimen width (mm)
c	bonded length (mm)
C_{1-4}	constants of integration (–)
E	tensile modulus of isotropic material (N/mm^2)
E_{a}	adhesive Young's modulus (MPa)
E_{adher}	adherend Young's modulus (MPa)
E_x^{f}	adherend bending modulus (MPa)
E_{xx}	UD lamina longitudinal, x-direction, modulus (MPa)
E_{zz}	UD lamina transverse, z-direction, modulus (MPa)
G_{a}	adhesive shear modulus (MPa)
G_{adher}	adherend shear modulus (MPa)
G_{Ic}	critical mode I fracture energy (N/mm)
$G_{\text{Ic,bi-mat}}$	critical mode I fracture onset energy of bi-material adhesive joint (N/mm)
G_{xz}	UD lamina shear modulus in xz-direction (MPa)
G_{xy}	UD lamina shear modulus in xy-direction (MPa)
G_{zy}	UD lamina shear modulus in zy-direction (MPa)
h	arm thickness in a homogeneous DCB specimen (mm)
h_{adher}	adherend thickness (mm)
h^*_{GFRP}	final thickness of the laminate after post-cure cycle
I	second moment of the beam cross-section area (mm^4)
k	foundation stiffness (MPa)
k_{a}	adhesive constant defining stress state (–)
k_{adher}	adherend constant defining stress state (–)
K	interface corner stress intensity factor ($\text{MPa}\sqrt{\text{mm}}$)
K_{I}	stress intensity factor of opening mode ($\text{MPa}\sqrt{\text{mm}}$)
K_{II}	stress intensity factor of shear mode ($\text{MPa}\sqrt{\text{mm}}$)
K_{I}^{∞}	remote mode I K-field ($\text{MPa}\sqrt{\text{mm}}$)
K_{1-4}	constants of integration (–)
L	specimen length (mm)
l_{e}	bonded region length in elastic regime (mm)
l_{f}	length between the loading point and the origin (mm)
l_{p}	plastic zone length (mm)
m_{q}	constant defining stress state in the adhesive (–)
P	applied load (N)
P_{c}	critical load at fracture onset (N)
$\tilde{P}$	normalized load (–)
$\tilde{P}_{\text{bi-mat}}$	normalized load of bi-material adhesive joint (–)
$\tilde{P}_{\text{c}}$	normalized critical load at fracture onset (–)
$\tilde{P}_{\text{c,bi-mat}}$	normalized critical load at fracture onset of bi-material adhesive joint (–)
r	radial distance from the crack tip (mm)
r_{p}	Irwin's estimate of the radius of the plastic zone (mm)
R_{1-2}	constants of integration (–)
S	equal to $\left(\frac{1}{E^{\text{f}}_{x-\text{steel}} I_{\text{steel}}} + \frac{1}{E^{\text{f}}_{x-\text{GFRP}} I_{\text{GFRP}}}\right)$ ($1/\text{MPa.mm}^4$)
T	stress acting parallel to the crack plane (MPa)
w	displacement in z-direction (mm)
$w_1(x)$	deflection in region 1 of Yamada's model (mm)
$w_2(x)$	deflection in region 2 of Yamada's model (mm)
$w_3(x)$	deflection in region 3 of Yamada's model (mm)
$2t_{\text{a}}$	adhesive bond-line thickness (mm)

Greek Symbols

α	Dundurs parameter (–)
β	Dundurs parameter (–)
γ	constant related to the order of singularity (–)
Δ	half-opening displacement in DCB specimen (mm)
Δa	pre-crack length (mm)
$\Delta a_{\text{crit.}}$	critical pre-crack length (mm)
$\Delta a_{\text{exper.}}$	experimental pre-crack length (mm)
Δa_{expmax}	maximum experimental pre-crack length (mm)
ε	oscillation index (–)
ε_{yy}	strain component in y-direction (–)
λ	wave number (mm^{-1})
λ^{-1}	elastic process zone length (mm)
ν_{a}	adhesive Poisson's ratio (–)
ν_{adher}	adherend Poisson's ratio (–)
ν_{xz}	UD lamina Poisson's ratio (–)
σ_{ultimate}	ultimate (maximum) strength (MPa)
σ_{xx}	stress component in x-direction (MPa)
σ_{yield}	adhesive yield strength (MPa)
σ_{yy}	stress component in y-direction (MPa)
σ_{yy}^{∞}	remote stress component in y-direction (MPa)
$\sigma_{yy-\text{homogeneous}}$	stress component normal to a crack in homogeneous material (MPa)
$\sigma_{yy-\text{interface}}$	stress component normal to bi-material interface (MPa)
σ_{xy}	stress component in xy-direction (MPa)
2Δ	total opening displacement in DCB specimen (mm)
$2\tilde{\Delta}$	normalized displacement (–)

Superscripts & subscripts

adher 1	adherend 1
adher 2	adherend 2
GFRP	GFRP adherend
steel	steel adherend

Acronyms

ASTM	American Society for Testing and Materials
CLT	Classical Laminate Theory
CTE	Coefficient of Thermal Expansion
DCB	Double-Cantilever Beam
DIC	Digital Image Correlation
FE	Finite Element
FEM	Finite Element Modelling
DW	Distilled Water
GFRP	Glass Fibre Reinforced Polymer
GPS	glycidoxypropyltrimethoxysilane
ISO	International Organization for Standardization
UD	Unidirectional

the DCB configuration has been modified and extended to cover the effects of various parameters (e.g. bond-line thickness or shear deformation of adherends). The name originates from the work of J.J. Benbow and F.C. Roesler [12], in which each arm of the specimen is treated as a built-in cantilever beam having a length equal to the length of the crack. The test and the data treatment incorporates easily measurable quantities - macroscopic displacement and external force, used to establish fracture driving parameters.

M.F. Kanninen [13] developed the "augmented DCB model" for crack propagation analysis of a homogeneous specimen as shown in Fig. 1(a). The model takes direct account of the region behind the crack by considering a finite length beam which is partially free (representing the unbonded part of the specimen) and partially supported by an elastic foundation (representing the bonded region). The mathematical description of the model is based on the simplest theories: the Euler-Bernoulli beam theory and the Winkler foundation. This model

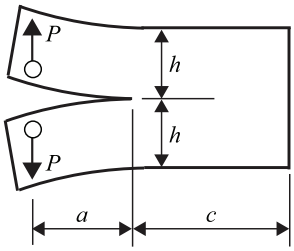

(a) M.F. Kanninen [13]: homogeneous DCB specimen modelled by considering a finite length beam which is partially free (Euler-Bernoulli beam) and partially supported by an elastic foundation (Winkler foundation).

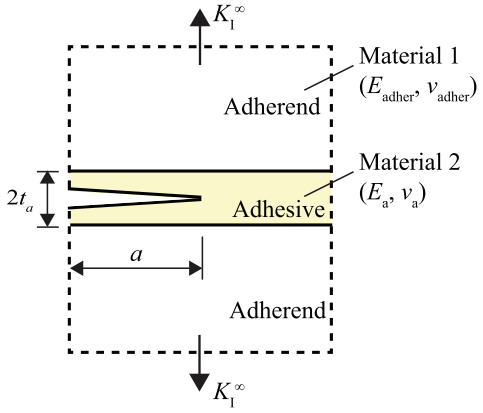

(b) F. Van Loock, M.D. Thouless, N.A. Fleck (2019) [14]: adhesive joint with semi-infinite crack subjected to a remote mode I K-field.

Fig. 1. Comparison of mode I geometries used to analyse adhesive joints.

remarkably gives information about the region in front of the crack, in particular the elastic process zone, λ^{-1}, which is interpreted as the distance (from the crack tip) over which the positive peel stress is distributed. Therefore, this model can form a phenomenological basis for cohesive zone models as crack tip opening displacements and stress are incorporated. However, this analysis, which can be considered as meso-scale, was intended for fracture of homogeneous materials and, therefore, did not include an adhesive layer. Later on, F.E. Penado extended M.F. Kanninen's analysis to adhesive joints, by including the adhesive layer in the analysis [15]. Moreover, S.E. Yamada modelled the bonded region by considering a beam on an elastic-plastic foundation [16].

At this stage, it seems reasonable to postulate that the limit of applicability of various models is related to the adhesive thickness. As the adhesive thickness tends to zero, like in laminated materials, either J.J. Benbow and F.C. Roesler [12] or M.F. Kanninen [13] approximations will suffice. For sufficiently thick bond-lines, local stress gradients should be expected, however, meso- and local-scale analysis should be used, such as F.E. Penado's and S.E. Yamada's analyses [15,16]. Finally, once adhesive thickness tends to infinity, in the presence of a embedded crack, stress intensity asymptotic analysis will be necessary [10].

Following the early works of J. Dundurs and D.B. Bogy [17,18], it has been recognized that the so-called basic interface problem (two dissimilar material bonded along shared interface under remote loading) introduces local stress gradients due to the material properties mismatch. Such singular stress field, in case of materials containing a crack, comes as complementary to the crack tip stress field.

In 1987, J.W. Hutchinson et al. [6] investigated competition between the crack tip singular field and materials mismatch induced stress gradient near the interface, leading to formulation of conditions for a sub-interface crack growth. Here, authors noted that the stable sub-interface crack growth is unlikely and once the crack front onsets in cohesive manner within any of the two joined materials, configurational (≡ directional) stability of the crack follows another criterion (Cotterell-Rice theory [19]). From this work, we learn that only a negative non-singular term at the crack tip (which refers specifically to the so-called T-stress explained at a later stage) can guarantee stable crack growth. The basic interface problem enriched by the presence of an interface crack was pursued by Z. Suo and J.W. Hutchinson [20,21]. The classic square root dependence of the stresses on the distance away from the crack tip remains, however, material mismatch enforces use of complex variables and adds additional term to the power dependence of the stress on the distance from the crack tip.

F. Van Loock et al. [14] studied adhesive joints subjected to a remote mode I K-field of magnitude K^∞. The joints, composed by an elastic adhesive layer of thickness $2t_a$ sandwiched between two elastic adherends, contained a semi-infinite crack as shown in Fig. 1(b). The normal stress component σ_{yy} distribution (perpendicular to the crack plane and within the adhesive layer) ahead of the crack tip was determined by finite element analysis for different values of modulus-mismatch ratio $\frac{E_a}{E_{adher}}$ (E_a and E_{adher} being the Young's modulus of the adhesive and adherend, respectively). σ_{yy} is shielded by the presence of stiffer adherend material. As the mismatch in modulus increases (decreasing $\frac{E_a}{E_{adher}}$), the stress distribution tends to the solution for a semi-infinite crack in an adhesive layer between two rigid adherends and subjected to an uniform opening displacement. The stress is predicted to be independent of crack length and decreases with an increase in bond-line thickness [22].

A certain gap between different approaches exists, specially when it comes to implementation into the DCB-like geometries where the bond-line is once used as a crack and once as containing the crack. In fact, the standard DCB treatment skips adhesive thickness (as in ASTM D 5528 [23]), implying that the same models could be used for thin and thick bond-lines. Use of composites and bonded materials is associated with carrying a bending-type of loading, while most of the geometries investigated use idealized, remotely applied tensile loading. Such approach ultimately omits important length scale introduced by bending as outlined by the analysis of M.F. Kanninen in [13]. The load acting over the crack region cannot be treated as uniform, contrary to the case of remotely applied tensile loading as in [14]. Effects of plastic radius are barely investigated within the outlined framework, however role of this region is known as critical [24].

The literature available shows that a proper analysis of DCB joints characterized by dissimilar materials and thick adhesive bond-lines with small crack length, which are representative of engineering applications, is missing. In the present paper, the geometry under consideration is shown in Fig. 2. Two adherends with finite thickness are bonded together with an adhesive of thickness $2t_a \approx 10$ mm. A pre-crack of length Δa is cut at mid-thickness of the adhesive bond-line. With such adhesive bond-line thickness, stress gradient arises at bi-material edges and corners. Length Δa plays a critical role on fracture onset locus in current approach. The definition of Δa follows the idealization of unloaded region of material adjacent to the crack surfaces

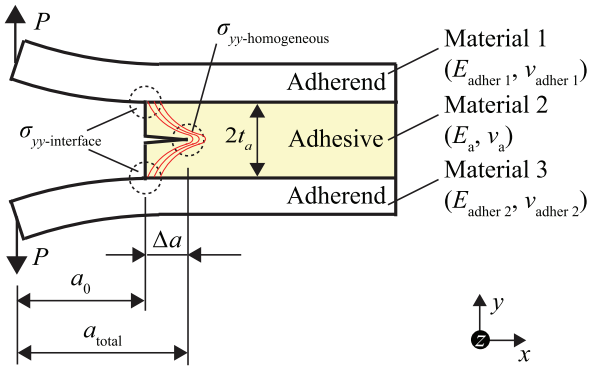

Fig. 2. Current approach: influence of Δa length on fracture onset in adhesive joint with finite thickness adherends under global mode I loading.

in an infinite homogeneous plate with a crack as postulated by A.A. Griffith [25,10]. The unloaded region is approximated by a triangle with the base length corresponding to Δa and a height of $2\pi\Delta a$. Δa must be sufficiently large so the corners near the interfaces are unloaded, as illustrated in Fig. 2 by the red diffusion lines. In other words, Δa must be sufficiently large to create a singular stress field around the pre-crack tip, in which the threshold stress is first attained rather than at bi-material edges and corners, resulting in fracture onset at the pre-crack tip.

The primary objective of this study is to investigate the fracture onset and crack deflection in adhesive joints with thick bond-lines (≈10 mm) under global mode I loading. More specifically, the role of adherend-adhesive modulus-mismatch and the role of pre-crack length, Δa, are scrutinized. The parameters controlling the crack path directional stability are also discussed. Single-material (i.e. steel-steel and GFRP-GFRP) and bi-material (i.e. steel-GFRP) DCB joints bonded with a structural epoxy adhesive are tested. The tests are aided by a 3D image acquisition system. Moreover, the fracture tests are modelled analytically by considering a beam on elastic-plastic foundation - S.E. Yamada [16], and numerically.

2. Experimental

2.1. Materials and preparation

2.1.1. Materials used

Fig. 3 shows the three DCB configurations tested. The adherends were made of either S690 steel, with a thickness of 3.0 mm, or glass fibre reinforced polymer (GFRP) laminate, with a thickness of 8.6 mm. The adherends were bonded with a structural two-component epoxy paste adhesive, Araldite 2015 (Huntsman®) with a bond-line thickness of 10 mm.

The GFRP laminate was manufactured with quadraxial E-glass fabric (nominal thickness of 0.9 mm), which consists of a stacking of four unidirectional (UD) layers of E-glass lamina with the orientations −45°/90°/+45°/0°. A rubber modified epoxy based vinyl ester resin was used to impregnate the E-glass fabric stacking sequence. The GFRP laminate was manufactured by vacuum infusion. After a period of 24 h at fv laboratory temperature (≈23 *degr*C), the laminate was post-cured at 60 °C during 12 h in an oven, following supplier's specifications. The mechanical properties of the UD-0° GFRP lamina were experimentally determined and are given in Table 1. The mechanical properties of the steel S690 and the epoxy adhesive are listed in Table 2. The steel properties were taken from the supplier's technical data-sheet, while the adhesive's mechanical properties were experimentally measured from tensile dog bone specimens with a thickness of 2 mm in accordance with ISO 527 [26].

2.1.2. Assumption concerning symmetry of the bi-material specimen

The bi-material steel-GFRP DCB specimens were manufactured by following the Strain Based Design criterion developed by W. Wang et al. [27] to guarantee pure mode I loading at the crack tip. The Strain based criterion is given by,

$$E_x^{\mathrm{f-adher1}} h_{\mathrm{adher1}}^2 = E_x^{\mathrm{f-adher2}} h_{\mathrm{adher2}}^2, \tag{1}$$

where $E_x^{\mathrm{f-adher1,2}}$ is the effective bending modulus of adherend 1 and 2, respectively. For the steel adherend, $E_x^{\mathrm{f-Steel}}$ is equal to material Young's modulus (see Table 2). The effective bending modulus of the GFRP laminate, $E_x^{\mathrm{f-GFRP}}$, is calculated by applying the classical lamination theory (CLT). More details in [28].

By considering the steel adherend thickness, h_{steel}, equal to 3 mm, the GFRP adherend is designed to meet the Strain based criterion. The lay-up of the GFRP laminate is given in Table 3 as well as $E_x^{\mathrm{f-GFRP}}$ and the final thickness of the laminate after post-curing (the final thickness is smaller than the nominal one due to the manufacturing process constraints).

2.1.3. Surface preparation and bonding

The surfaces of the steel adherends were grit blasted using aluminium oxide (Corublast Super Z-EW nr. 100). Before and after the grit blasting, the surfaces were cleaned with a clean cloth soaked with acetone. Afterwards, the steel surfaces were immersed in a potassium hydroxide solution (alkaline cleaner), which was stirred at 300 rpm and heated to 60 °C. The immersion in the solution lasted 10 min. As a final step prior to bonding, the cleaned steel surfaces were immersed in a silane γ-glycidoxypropyltrimethoxysilane (γ-GPS) solution for 20 s in order to strengthen the adhesion of the adhesive at the interfaces. The steel adherends were then oven cured for 1 h at 150 °C. The silane solution was prepared in three steps according to G. Li et al. [29]. Firstly, the γ-GPS was hydrolysed in distilled water (DW)-methanol mixture. The volume ratios of γ-GPS/DW/methanol were 10/80/10, respectively. Secondly, the pH was set to 5–5.5 by adding acetic acid to keep the solution's stability. Finally, the solution was magnetically stirred for 48 h at 300 rpm at room temperature.

The surfaces of the GFRP laminate were manually abraded with sandpaper (grid 180). During this process, care was taken to not affect the fibres of the laminate. Before and after the sanding, the GFRP surfaces were cleaned with a clean cloth soaked with isopropanol.

A manual applicator gun with a static-mixing nozzle was used to mix and apply the two-component epoxy paste adhesive, Araldite 2015. In order to have a correct mixture of both components, a small quantity of adhesive was first discarded. Metallic spacers of approximately 10 mm were used to obtain a uniform adhesive bond-line, as shown in Fig. 3. Two metallic strips and a sharp razor blade were used to build the spacers. These components were bonded by a fast curing adhesive. While the metallic strips designated the length of initially unbonded zone and the distance from the load application point - a_0, the razor blade placed in between the metallic strips created an additional pre-crack of length Δa at the mid thickness of the adhesive bond-line - see Fig. 3. To facilitate post-bonding removal, the spacers were covered with a release agent. After the bonding process, curing took place at 80 °C for 1 h according to manufacturer's specifications. An even bond-line thickness was obtained by making use of weights to uniformly compress the specimens. After curing the specimens, the excess of adhesive on the sides was removed by abrasion. In some cases, the length Δa of the existing pre-crack was extended. The total thickness of the specimens was measured at three locations along the specimen length and the average was calculated in accordance with the ASTM D5528-13 [23]. Finally, prior to testing, to enable Digital Image Correlation (DIC) evaluation, a thin layer of white paint was applied to the side of the specimens with the black speckles painted on top.

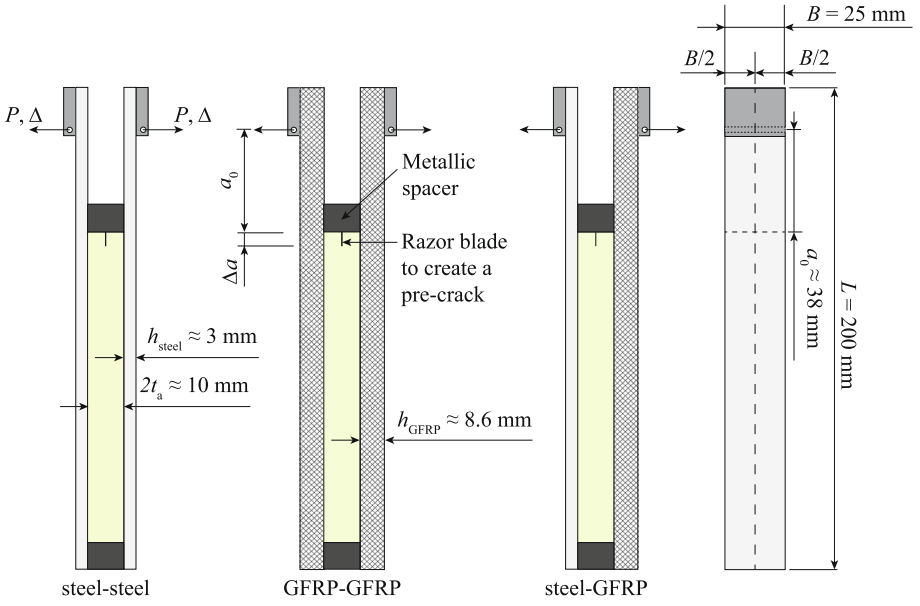

Fig. 3. DCB specimen: the three tested configurations.

Table 1
Mechanical properties of the UD-0° GFRP lamina.

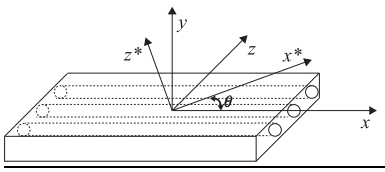

Material	E_{xx} (MPa)	$E_{zz} = E_{yy}$ (MPa)	G_{xz} (MPa)	G_{xy} (MPa)	G_{zy} (MPa)	ν_{xz}
UD-0° GFRP lamina	37861	12047	5003	4125	3692	0.252

Table 2
Mechanical properties of steel S690 and epoxy adhesive Araldite 2015.

Material	E (MPa)	ν	σ_{yield} (MPa)	$\sigma_{ultimate}$ (MPa)
Steel S690	210000	0.30	770	832
Epoxy adhesive*	2000 ± 300	0.33**	16.1 ± 1.9	28.8 ± 0.7

Steel: yield strength 0.2% offset; Adhesive: yield strength 0.1% offset.
* experimentally measured from dog bone specimens cured 1 h at 80°C
** supplier's technical data-sheet

Table 3
GFRP laminate: lay-up based on the Strain based design criterion [27] (the lay-up is defined from the bottom to the top of the laminate).

Criterion	Lay-up	h^*_{GFRP} (mm)	E_x^{f-GFRP} (MPa)
Strain based	$[0° \ +45° \ 90° \ -45°]_5/[+45° \ 90° \ -45° \ 0°]_5$	8.60	21996

h^*_{GFRP} – final thickness of the laminate after post-cure cycle.

2.2. Test set-up

The mode I fracture energy was determined from the DCB test. The DCB specimens were tested in a Zwick tensile test machine, equipped with a 20 kN load cell (precision of 0.5%) under the displacement rate of 1 mm/min. The tests were carried out to failure at laboratory conditions (temperature of 23 °C and relative humidity of 55%). The 3D image acquisition system was placed at the side of the specimen (VIC-3D system by Correlated Solutions, Inc.) with pictures taken every second after the load application. Four to five specimens per joint configuration were tested.

The reason to use the 3D image acquisition system was twofold: (i) monitoring of the crack growth throughout the test and, (ii) to obtain full-field displacement and strain fields over the specimen's surface using DIC technique. The speckle images were processed using Vic-3D 8 software. A parametric study of the effect of the subset and step size on the displacement and strain results was performed. The subset size was set to 29 and the step size was set to 7 pixels. The crack length was defined as the straight and horizontal line distance between the load line and the crack tip, where the load line is supposed to be coincident with the centre-line of the grips' pins. Moreover, it was assumed that any displacement occurring in the end-blocks is negligible compared to the displacement of the arms of the specimens.

3. Modelling methods

3.1. Beam on elastic-plastic foundation

Incorporating relevant length scales, the adhesive thickness, the elastic stress field and the plastic fields can be tedious when using full three dimensional continuum approach. Instead, this work will use an extension of the known Kanninen model [13] for the DCB geometry. S. E. Yamada [16] extended Kanninen's model by including adhesive plasticity effects at the crack tip. We follow his model assuming elastic/perfectly plastic response of the adhesive while the beam remains elastic. The physical model and mathematical formulation are split into three domains/regions as seen in Fig. 4:

- Region 1, (deflection w_1), is the free part of the beam;
- Region 2, (deflection w_2), is the part of the beam which is supported by a perfectly plastic foundation due to the yielding of the adhesive. The stress condition at the crack tip is dominated by a vertical component. Therefore, within the plastic zone, an uniform uni-axial stress is assumed;
- Region 3, (deflection w_3), is the part of the beam which is supported by an elastic foundation.

The DCB specimen is assumed to be symmetric about the x-axis along the centre-line of the adhesive layer. Only half of the specimen is represented in Fig. 4 (bond-line of thickness t_a).

The governing equations of the structural response are,

$$E_x^f I \frac{d^2 w_1}{dx^2} = P(l_f + x),\ -l_f \leqslant x < -l_p \tag{2}$$

$$E_x^f I \frac{d^4 w_2}{dx^4} = -\sigma_y B,\ -l_p \leqslant x < 0 \tag{3}$$

$$E_x^f I \frac{d^4 w_3}{dx^4} = -k w_3,\ 0 \leqslant x < l_e \tag{4}$$

in which $E_x^f I$ is the bending stiffness of the beam ($I = \frac{B h_{adher}^3}{12}$, being h_{adher} the thickness of the beam), w_i is the deflection in region i ($i = 1, 2, 3$), x is the location in reference to the boundary of elastic and plastic regions, l_f is the length between the loading point and the origin, l_p is the plastic zone length, P is the applied force, σ_y is the yield strength of the adhesive, B is the width of the specimen. Finally, k is the foundation stiffness defined by,

$$k = m_q \frac{E_a B}{t_a}, \tag{5}$$

where m_q is parameter of order one, t_a is the thickness of the foundation (half the thickness of adhesive bond-line), E_a is the Young's modulus of the adhesive. Constant m_q ($q = 1, 2$) allows for arbitrary formulation of the stress state at the crack tip. Specifically, m_q is expressed as,

$$m_1 = 1, \tag{6}$$

assuming plane-stress in both out-of-plane and in-plane directions [30],

$$m_2 = \frac{(1 - \nu_a)}{(1 - 2\nu_a)(1 + \nu_a)}, \tag{7}$$

assuming plane-strain in both out-of-plane and in-plane directions [31], where ν_a is the Poisson's ratio of the adhesive.

The solution to the differential equations reads as,

$$w_1(x) = \frac{P}{6E_x^f I}x^3 + \frac{P l_f}{2E_x^f I}x^2 + R_1 x + R_2, \tag{8}$$

$$w_2(x) = -\frac{\sigma_y B}{24E_x^f I}x^4 + \frac{C_1}{6}x^3 + \frac{C_2}{2}x^2 + C_3 x + C_4, \tag{9}$$

$$w_3(x) = K_1 \cos(\lambda x)\cosh(\lambda x) + K_2 \cos(\lambda x)\sinh(\lambda x) + K_3 \sin(\lambda x) \times \sinh(\lambda x) + K_4 \sin(\lambda x)\cosh(\lambda x), \tag{10}$$

with $R_{1-2}, C_{1-4}, K_{1-4}$ being constants of integration to be found through a boundary value problem and in which λ, defined by,

$$\lambda^4 = \frac{k}{4E_x^f I}, \tag{11}$$

is the wave number, the inverse of which defines the elastic process zone length. The process zone length, λ^{-1}, in the context of the elastic foundation is interpreted as the distance (from the crack tip) over which the positive peel stress is distributed. The λ^{-1} length exits beyond of the crack tip due to finite rigidity of the adhesive. Expanding and substituting for k and I, Eq. 11 can be rewritten in a non-dimensional form as,

$$\lambda^4 t_a h_{adher}^3 = 3 m_q \frac{E_a}{E_x^f} \tag{12}$$

which reveals the relation between the bonded structure characteristic length scales (left hand side) and adherend/bond-line material mismatch (right hand side).

The results of the constants of integration and the plastic zone length for the case where the bonded region is sufficiently long appear in Appendix I. Please note that once l_p approaches zero in Eqs. (2)–(4), the problem turns into elastic foundation only, i.e. M.F. Kanninen model [15]. Additionally, once l_e approaches zero, there will be no characteristic length λ^{-1} and the beam is treated as fixed at the crack tip like in J.J. Benbow and F.C. Roesler studies [12].

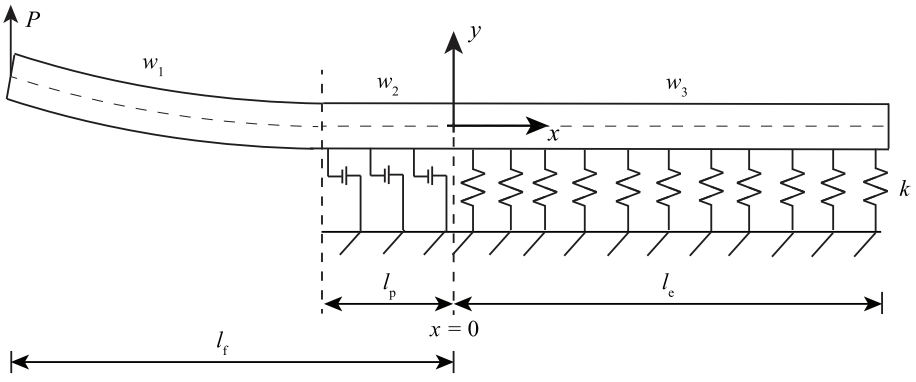

Fig. 4. DCB specimen modelled according to S.E. Yamada's model [16]: elastic-plastic foundation.

3.2. Finite element (FE) model

The proposed analytical methodology is aimed in indicating and including characteristic length scales of the problem. However, the problem at hand involves additional, local phenomena of three dimensional (3D) nature such as corners, beyond its capability and intention. While the asymptotic analysis is involved later for discussion, for better comprehension a 3D numerical model of the DCB bonded joints was built in Abaqus®. The joints were modelled using 8 node linear brick elements (C3D8). The adherends were modelled as linear elastic, using the material properties given in Tables 1 and 2. The adhesive was modelled as elastic-plastic, using the input data from R.L. Fernandes et al. [32]. The number of elements through-the-thickness direction of the GFRP adherends was defined by one element per lay-up layer. For the steel adherends, 10 elements were used in thickness direction. When needed, a seam crack embedded in the adhesive part was included in the model. The mesh was refined in the areas of interest, i.e. crack tip region and adherend-adhesive interfaces. A coarser mesh was applied in the rest of the model. A mesh convergence study was performed to guarantee mesh independency of the numerical results. In order to simulate the real constraints during a DCB test, the following boundary conditions and loading were applied: 1) the left end of the lower edge of the bottom adherend was constrained from all displacements, rotations were not constrained; 2) the left end of the top edge of the top adherend was constrained from displacement in longitudinal direction; 3) a load was applied on the left end of the upper edge of the top adherend, equal to the load taken from the experimental tests. A mesh overview with the applied boundary conditions is shown in Fig. 5.

4. Experimental results and models validation

4.1. Normalized load vs. displacement curves: stiffness during loading

Fig. 6(a), (c) and (e) show the representative load vs. displacement ($P-2\Delta$) curves of the three tested configurations: steel-steel, GFRP-GFRP and steel-GFRP, respectively. Two curves for different values of Δa are presented per joint configuration because length Δa influences fracture onset locus. In each configuration, the difference in specimens' compliance is expected as the initial total crack length, $a_{0\text{total}} = a_0 + \Delta a$, as shown in Fig. 2, is not the same in all specimens. Moreover, $a_{0\text{total}}$ also affects the maximum load of each specimen. The load-displacement curves show an initial linear region, followed by a smooth transition before crack propagation. This transition is result of plastic effect. The propagation region is initially characterized by a drop on the applied load. After that, the load decreases gradually with increasing displacement up to final failure. The smooth propagation region gives evidence that the fracture process zone was similarly throughout the test.

In addition, Fig. 6(b), (d) and (f) show the normalized load vs. displacement ($\tilde{P}-2\tilde{\Delta}$) curves of the three tested configurations. For the sake of simplicity, the normalization is performed by following the simple beam theory [23]. The shear deformation of the adherends is also included. The shear effect is specially important for the GFRP adherends as the ratio $\frac{a_{0\text{total}}}{h_{\text{GFRP}}}$ is approximately 4, which corresponds to the stubby beam geometry, whilst its value is higher than 10 when considering the steel adherend. The load and displacement normalization is given by,

$$\tilde{P} = \frac{2Pa_{0\text{total}}^2}{3E_x^{\text{f}}I} + \frac{3P}{BG_{\text{adher}}h_{\text{adher}}}, \tag{13}$$

$$2\tilde{\Delta} = \frac{2\Delta}{a_{0\text{total}}}, \tag{14}$$

where G_{adher} is the shear modulus of the adherend. In the bi-material joints, the bending stiffness of both adherends must be taken separately,

$$\tilde{P}_{\text{bi-mat}} = \frac{Pa_{0\text{total}}^2}{3}S + \frac{3P}{2BG_{\text{steel}}h_{\text{steel}}} + \frac{3P}{2BG_{\text{GFRP}}h_{\text{GFRP}}}, \tag{15}$$

where S is given by,

$$S = \frac{1}{E_x^{\text{f-steel}}I_{\text{steel}}} + \frac{1}{E_x^{\text{f-GFRP}}I_{\text{GFRP}}}. \tag{16}$$

This normalization allows the comparison of initially linear part of the experimental curves with any other bonded joints, regardless the materials and joint geometry (for instance, $a_{0\text{total}}$ length and adherends thickness), so that differences between the observed and calculated slopes can be attributed to the finite through-the-thickness stiffness of the adherend and the adhesive bond-line [15], as these parameters are not taken into consideration in the performed normalization.

The normalized curves of the experimental steel-steel and steel-GFRP bonded joints show the same initial slope, regardless of the initial crack length, as expected [Fig. 6(b) and (f), respectively]. In the GFRP-GFRP bonded joints [Fig. 6(d)], the trend is different and the slopes of the initial linear part of the curves do not overlap. In fact, this result is unexpected. The only reason found for the difference is the presence of a kink in the initial linear part of the curve.

In Fig. 6(b), (d) and (f), the linear part of $\tilde{P}-2\tilde{\Delta}$ curves with the highest Δa is compared with the linear part of the results obtained

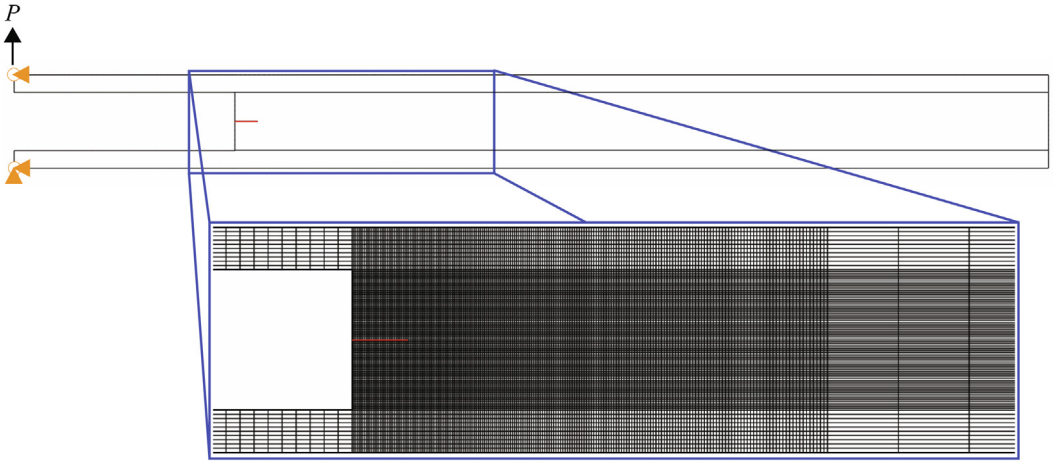

Fig. 5. Typical mesh details with applied boundary conditions (steel-steel joint as an example).

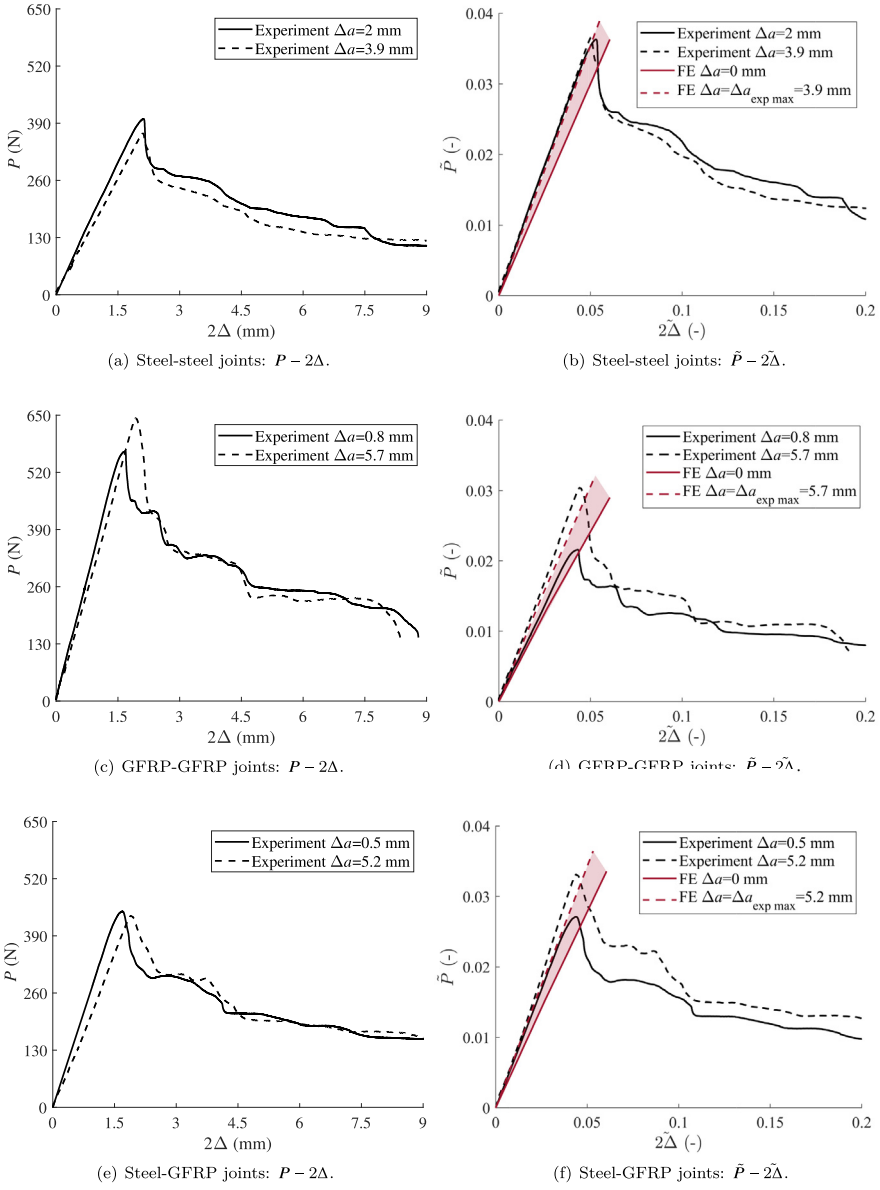

(a) Steel-steel joints: $P-2\Delta$. (b) Steel-steel joints: $\tilde{P}-2\tilde{\Delta}$.

(c) GFRP-GFRP joints: $P-2\Delta$. (d) GFRP-GFRP joints: $\tilde{P}-2\tilde{\Delta}$.

(e) Steel-GFRP joints: $P-2\Delta$. (f) Steel-GFRP joints: $\tilde{P}-2\tilde{\Delta}$.

Fig. 6. Experimental load vs. displacement curves: raw ($P-2\Delta$) and normalized results ($\tilde{P}-2\tilde{\Delta}$).

from the finite element analysis. Although there is a better agreement between the experimental and numerical results of the steel-steel joints, the difference between the experimental and numerical results in the other two configurations is less than 15%. Moreover, FE results for the case $\Delta a = 0$ mm are also plotted in Fig. 6(b), (d) and (f). This way, one can observe the spectrum of the structural response of the adhesive joints from $\Delta a = 0$ up to $\Delta a = \Delta a_{\text{expmax}}$, where Δa_{expmax} is the largest Δa experimentally implemented.

4.2. Normalized critical force at fracture onset

The critical force at fracture onset, P_c, is analysed and a normalization is performed, being the critical force equal to the maximum load, $P_{\max}$. Distinction is made between cohesive and close to interface fracture onset - see Fig. 7, regardless of joint configuration. The normalization is done by following the simple beam theory [23,32]. The critical fracture onset energy, G_{Ic}, and normalized $P_c, \tilde{P}_c$, are given by,

$$G_{Ic} = \frac{P_c^2}{BE_x^f I}\left(\frac{3\Delta E_x^f I}{P_c}\right)^{\frac{2}{3}}, \tag{17}$$

$$\tilde{P}_c = \frac{P_c.a_{0\text{total}}}{\sqrt{G_{Ic}BE_x^f I}}. \tag{18}$$

For the bi-material joints,

$$G_{Ic,\text{bi-mat}} = \frac{P_c^2}{2B}.S\left(\frac{2\Delta}{\frac{P_c}{3}.S}\right)^{\frac{2}{3}}, \tag{19}$$

$$\tilde{P}_{c,\text{bi-mat}} = \frac{P_c.a_{0\text{total}}}{\sqrt{2G_{Ic}B}}.\sqrt{S}. \tag{20}$$

Fig. 8 shows the critical force at fracture onset [Fig. 8(a)] and the normalized critical force [Fig. 8(b)] as a function of bond-line thickness. The results for the bond-line thickness range 0.4–4 mm were

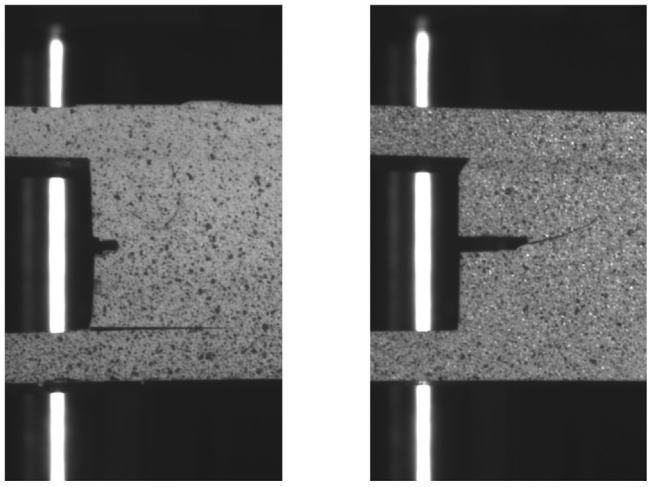

(a) Close to interface fracture onset. (b) Cohesive fracture onset.

Fig. 7. Fracture onset locus.

taken from R.L. Fernandes et al. [32,28]. This normalization allows the comparison of fracture onset, regardless the material and geometric properties of adhesive joints.

Similar values of $\tilde{P}_c$ are observed in Fig. 8(b), regardless of the bond-line thickness and fracture onset type. Looking into more detail to the results of adhesive joints with approximately 10 mm thick bond-line, the $\tilde{P}_c$ difference between cohesive and close to interface fracture onset is, in average, less than 10%. The similar results of $\tilde{P}_c$ indicate that the adhesive was able to deform as a response to the external loading, even though in some cases the critical stress was first attained in a region close to one of the adherend-adhesive interfaces due to materials modulus-mismatch ratio, as it is explained in a later stage. Moreover, these results also show that the surface pre-treatments were suitable and led to good adhesion at the interfaces, without interfering with the overall performance of the joints, i.e no adhesive failure occurred.

4.3. Deflection in bonded region

To evaluate the applicability of Yamada's model (meso-/process zone scale - see Fig. 4) and to further validate the FE models, the experimental deflection curves in the bonded region are compared with the analytical and numerical results. The experimental results are obtained by the DIC technique with pictures taken from the region close to the adherend-adhesive interfaces. Figs. 9 and 10 show curves representative for the steel-steel specimens with $\Delta a = 2$ and 3.9 mm, respectively, Figs. 11 and 12 show the deflection curves representative for the GFRP-GFRP and steel-GFRP specimens with $\Delta a = 5.7$ and 5.2 mm, respectively, corresponding to the two different stages of loading: the linear elastic region, and at the moment of fracture onset, i.e. at the maximum load. Both plane-stress and plane-strain conditions are considered in the analytical model [Eqs. 6 and 7], while the numerical results are taken from both the side and the centre ($B = \pm 12.5$ mm

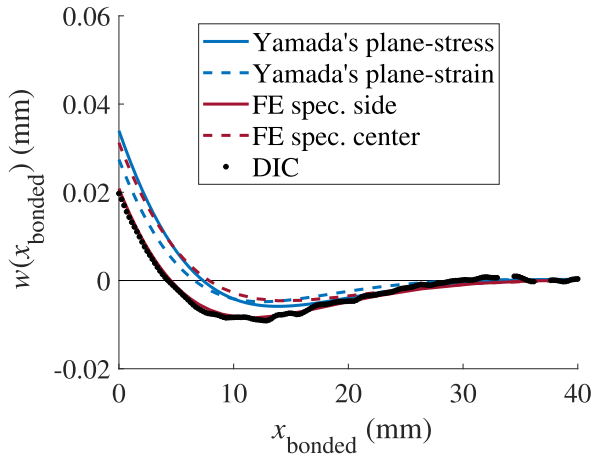

(a) Linear elastic region.

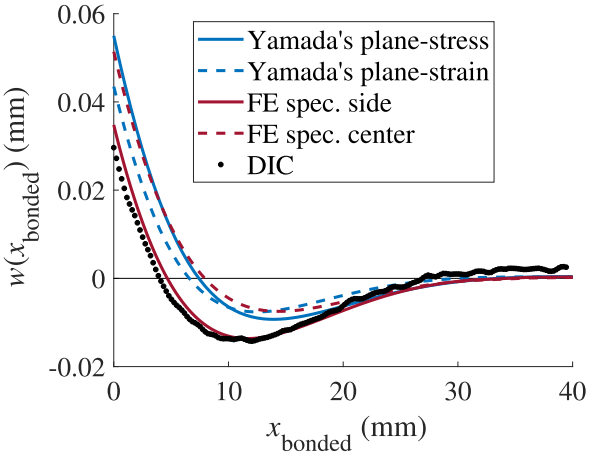

(b) Fracture onset moment.

Fig. 9. Deflection in bonded region of steel-steel joint: $\Delta a = 2$ mm.

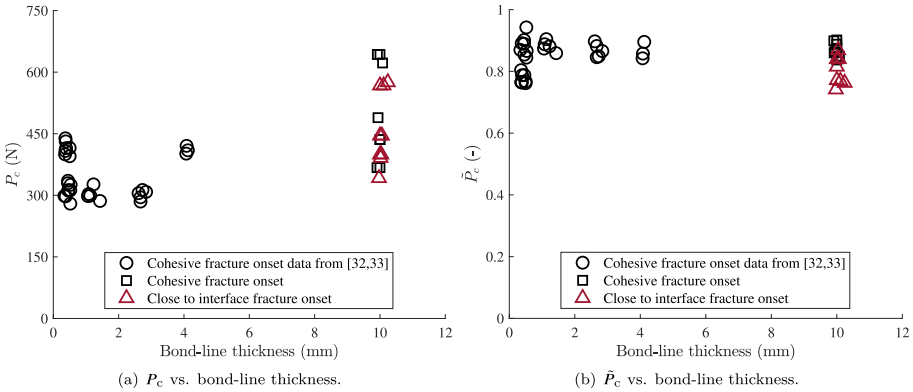

(a) P_c vs. bond-line thickness. (b) $\tilde{P}_c$ vs. bond-line thickness.

Fig. 8. Critical load, P_c, vs. normalized critical load, $\tilde{P}_c$, as a function of bond-line thickness.

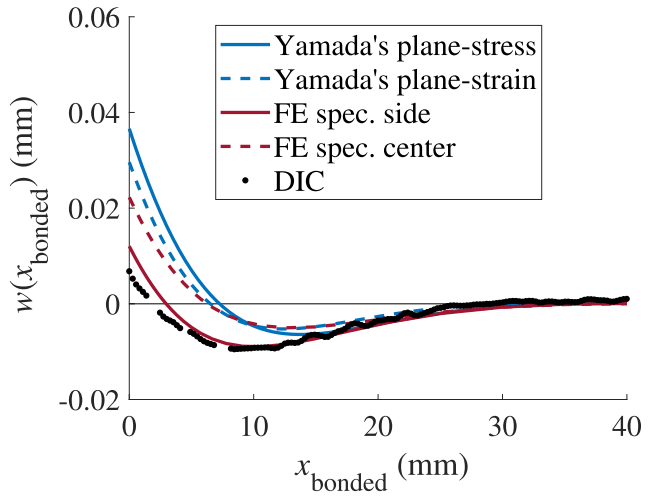

(a) Linear elastic region.

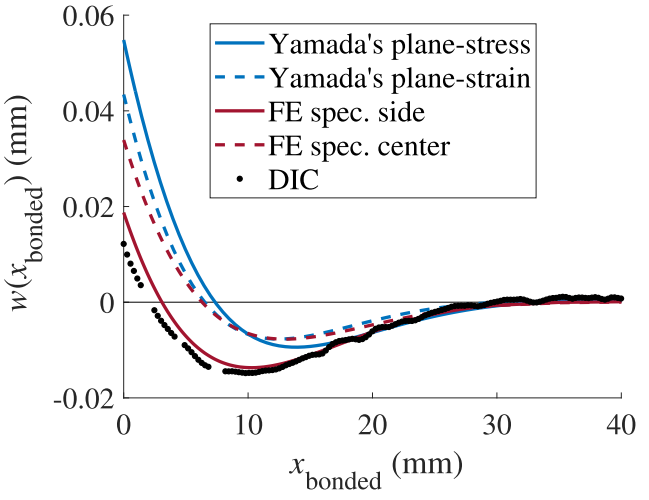

(b) Fracture onset moment.

Fig. 10. Deflection in bonded region of steel-steel joint: $\Delta a = 3.9$ mm.

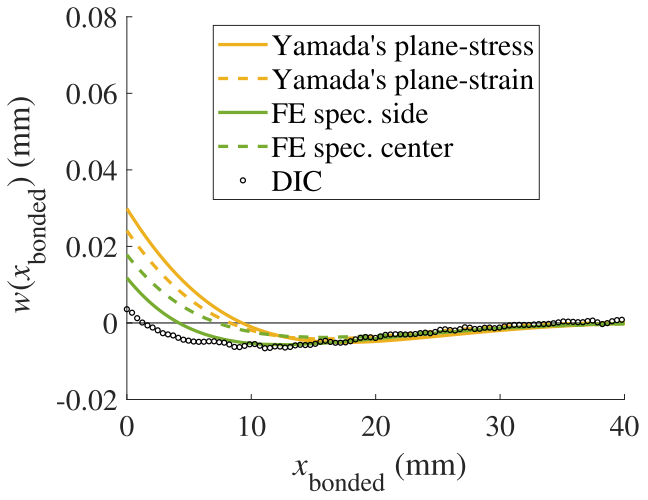

(a) Linear elastic region.

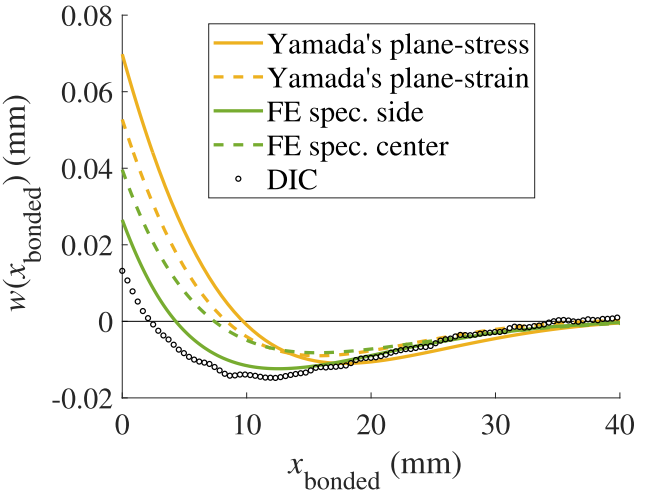

(b) Fracture onset moment.

Fig. 11. Deflection in bonded region of GFRP-GFRP joint: $\Delta a = 5.7$ mm.

and $B = 0$ mm, respectively) of the model at the adherend-adhesive interfaces. The curves are shifted from $x = -l_p$ to $x = 0$ for visualization purpose.

The agreement between different approaches is very encouraging, specially that no parameter fitting or adjustment was performed and entire models rely on properties measured through either tensile or bending testing of constituents. Besides, both the analytical and the FE models are based on a single value of the crack length, which cannot be treated as unique due to the crack front curvature [33–35] established at the fracture onset. Excellent agreement is observed between the experimental DIC and the FE results once comparing deflection as evaluated at the specimen side. At the same time, a very good agreement exists between the FE results for deflection along the specimen centre-line and the analytical model. The analytical results considering plane-stress conditions are higher than when considering plane-strain conditions. In the plane-stress case, in general, the adhesive bond-line appears too "soft". Please note that the plane-strain and plane-stress conditions are only applied to the adhesive. Effects, such as anticlastic curvature of the adherends, are not included in the analytical model.

One can observe that the analytical model stays in better agreement with the experimental deflection in bonded region for smaller values of Δa [Fig. 9]. In fact, the analytical model does not consider Δa (i.e. it does not take into account the fact that Δa is inside the thick bond-line) and local effects due to Δa, and thus, in general, the crack front stress singularities cannot be captured. Therefore, the case of $\Delta a = 0$ corresponds to the "foundation" representation. Here, however, one need to acknowledge, that such effects should be limited due to the development of the plastic zone at the crack tip.

5. Discussion

5.1. Fracture onset

5.1.1. The role of adherend-adhesive modulus-mismatch

In an adhesive joint with dissimilar adherends, in the case of near-surface fracture onset, the adherends-adhesive modulus-mismatches dictate the point of fracture initiation, i.e. the fracture onset locus is determined by the highest adherend-adhesive modulus-mismatch [36,37].

At the adherend-adhesive edge, singular stress is produced due to material mismatch and the threshold value is dependent upon material and geometrical properties, as shown by J. Dundurs and D.B. Bogy

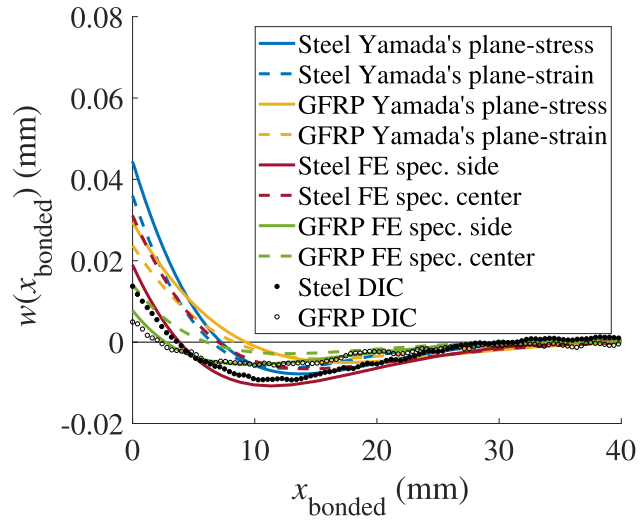

(a) Linear elastic region.

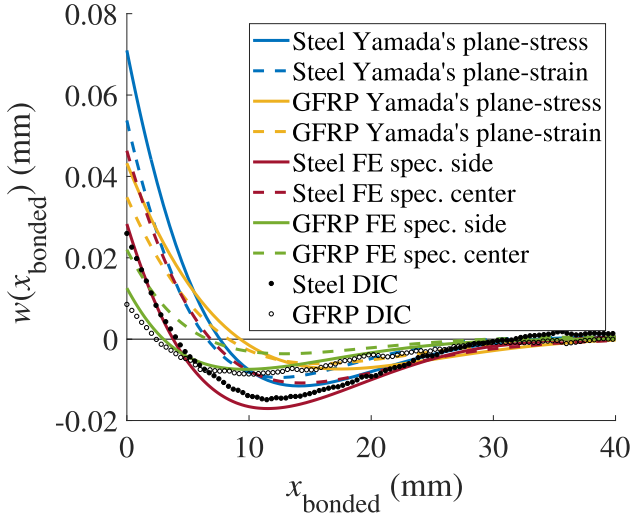

(b) Fracture onset moment.

Fig. 12. Deflection in bonded region of steel-GFRP joint: $\Delta a = 5.2$ mm.

[38,5]. The material mismatch is evaluated from Dundurs parameters α and β, which are given by,

$$\alpha = \frac{G_{\text{adher}}(k_{\text{a}}+1) - G_{\text{a}}(k_{\text{adher}}+1)}{G_{\text{adher}}(k_{\text{a}}+1) + G_{\text{a}}(k_{\text{adher}}+1)}, \tag{21}$$

$$\beta = \frac{G_{\text{adher}}(k_{\text{a}}-1) - G_{\text{a}}(k_{\text{adher}}-1)}{G_{\text{adher}}(k_{\text{a}}+1) + G_{\text{a}}(k_{\text{adher}}+1)}, \tag{22}$$

where the subscripts 'adher" and "a" refer to the materials for the adherend and adhesive, respectively. G_{adher} and G_{a} are the shear moduli, $k_i = 3 - 4\nu_i$ for plane strain and $k_i = (3-\nu_i)/(1+\nu_i)$ for plane stress (ν_i are the Poisson's ratios with i = adher, a). The parameter α can be interpreted as a measure of the dissimilarity in stiffness of the two materials. The adherend material is rigid relative to the adhesive as $\alpha > 0$ and compliant as $\alpha < 0$. The parameter β, as will be clear soon, is responsible for the near-crack tip oscillatory behavior at the bi-material interface [7].

There have been a lot of studies on the characterisation of the stresses at the adherend-adhesive corners of various joint geometries [5–9]. Within the framework of linear elasticity, the stress component normal to the bi-material corner of many adhesive joints is of the form,

$$\sigma_{yy-\text{interface}} = Kr^{\gamma-1} \ (r \to 0), \tag{23}$$

where r is the radial distance from the corner, K is the interface corner stress intensity factor and the $\gamma - 1$ is the order of the singularity. Please note that only the leading term is presented as only the crack tip region is of interest. Both K and γ depend on geometric and material properties of the joint. An increase of the singular stress is expected with a large mismatch between the two materials [9,37]. Depending on joint configuration, γ can be real or complex. For the problem of a crack at the interface between two dissimilar homogeneous materials, $\gamma = 1/2 + i\varepsilon$ [6,7], resulting in,

$$\sigma_{yy-\text{interface}} = \Re(Kr^{-1/2+i\varepsilon}), \tag{24}$$

$$\varepsilon = \frac{1}{2\pi}\ln\left(\frac{1-\beta}{1+\beta}\right). \tag{25}$$

Please note that Eqs. 23 and 24 are brought here to only illustrate how the stress field is affected by the materials mismatch at bi-material interfaces (parameter ε defined in Eq. 25).

In the special case of $\beta = 0$, the stress component normal to the crack tip has exactly the same form as that for homogeneous materials, i.e.,

$$\sigma_{yy-\text{homogeneous}} = Kr^{-1/2}. \tag{26}$$

Although experimental evidence corroborates the effect of the modulus-mismatch, as reported in R.L. Fernandes et al. [28], FE analysis was carried out to further investigate this effect. Three adhesive joints were modelled: steel-steel, GFRP-GFRP and steel-GFRP with adhesive bond-line of 10 mm. For comparison, two important features were kept the same in all models, i.e. no pre-crack in the adhesive layer ($\Delta a = 0$ mm) and same applied load (P_{c} of representative steel-steel joint with $\Delta a = 2$ mm, close to interface fracture onset).

The strain ε_{yy} contours of the three models are shown in Fig. 13. The adhesive joints with two equal adherends show symmetric strain distribution, having the highest strain values at the corners as shown in Fig. 13(a) and (b). However, in the case of dissimilar adherends, the strain distribution is not symmetric and the highest strain values are found in the region close to the adherend-adhesive interface with the higher modulus-mismatch, i.e. steel-adhesive interface as can been seen in Fig. 13(c). In fact, the steel-adhesive modulus ratio is 105, while a ratio of approximately 6 is obtained when considering the GFRP adherend.

The Dundurs parameters for each adherend-adhesive pair are listed in Table 4. Due to the adhesive bond-line thickness, the joint response to external loading is dominated by the adhesive and, thus, the adhesive plays a major role in the fracture onset process. Therefore, plane-strain conditions are considered. The positive α values show that both adherends are stiffer than the adhesive. As typically, β is approximately $\alpha/4$. As aforementioned, an increase of the singular stress is expected with a large mismatch between the two materials [9,37]. Therefore, the steel-epoxy interface is more prone to failure under condition that $\Delta a = 0$, as both Dundurs parameters are higher for this pair of materials. This is corroborated by the results in Fig. 13(c) and by experimental evidence. In the steel-GFRP adhesive joints, for the cases of close to interface fracture onset, the locus of failure was always nearby the steel-adhesive interface. More on that later in sub-Section 5.2.2.

5.1.2. The role of pre-crack length, Δa: crack tip singularity, diffusion lines and corner singularities

As explained in sub-Section 2.1.3, a pre-crack of length Δa is created during the bonding procedure at the mid-thickness of the adhesive bond-line in all specimens. The total crack length is equal to

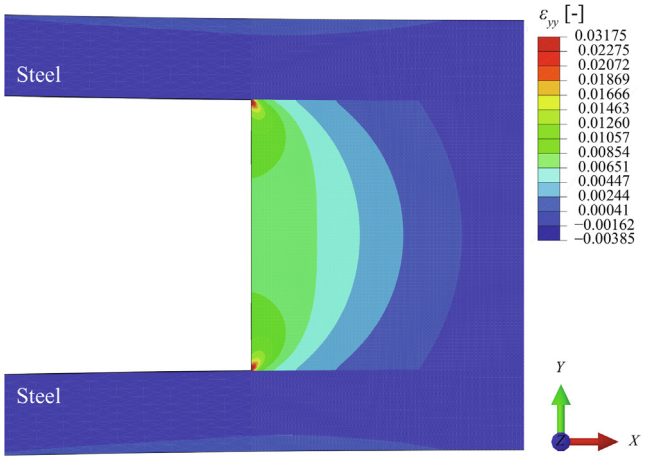

(a) Steel-steel adhesive joint.

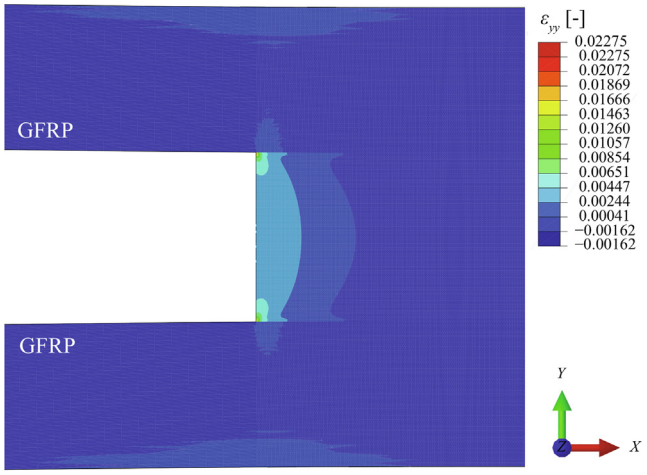

(b) GFRP-GFRP adhesive joint.

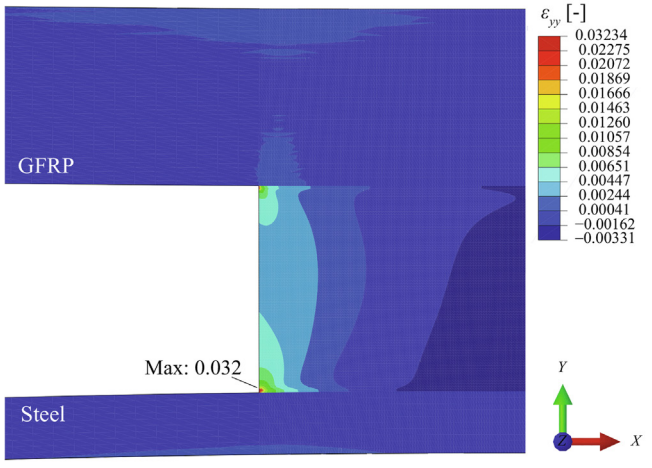

(c) Steel-GFRP adhesive joint.

Fig. 13. Evolution of strain field, ε_{yy}, for different adhesive joint configurations and corresponding adherends-adhesive modulus-mismatches. No pre-crack is modelled, $\Delta a = 0$ mm, and same load is applied in all models. The results are taken along the mid-width of the model ($B = 0$ mm).

a_{total} and it is defined as the straight and horizontal line distance between the P load line and the pre-crack tip, as illustrated in Fig. 2.

The fracture onset is dominated by the singular stress field around the existing pre-crack tip up to a certain bond-line thickness. For higher bond-line thicknesses, geometric discontinuities, such as corners, and material discontinuities, such as adherend-adhesive interfaces, create local singularities where the threshold stress is attained first. To overcome this situation, a critical pre-crack length must be defined, $\Delta a_{\text{crit.}}$.

As postulated by A.A. Griffith [10], when a crack has grown into a homogeneous solid to a specific depth, a region of material adjacent to the free surfaces is unloaded. The criterion to define Δa should be similar to Griffith's diffusion line approach, i.e. Δa must be sufficiently large so the corners near the interfaces are unloaded, as illustrated in Fig. 2 by the red diffusion lines. In other words, Δa must be sufficiently large so the stress threshold is first attained at the crack tip than at the corners. In the infinite plate with a crack, the unloaded region is approximated by an triangle with the base length corresponding to Δa and a height of $2\pi\Delta a$ [25]. This, for the problem at hand, would imply that as long as the adhesive thickness fulfil the criterion $2t_a \geqslant 2.(2\pi\Delta a)$, the corners are unloaded and the crack can only onset from the crack tip. It is clear that the critical length Δa depends on the bond-line thickness.

Therefore, the effect of the length of Δa on the fracture onset locus was experimentally investigated. Two types of bonded joints with 10 mm thick adhesive bond-line were studied: 1) single-material: steel-steel and GFRP-GFRP, 2) bi-material: steel-GFRP. Fig. 14 shows three examples of specimens with different Δa lengths and the corresponding strain, ε_{yy}, contours at fracture onset are shown in Fig. 15. Regardless of the joint type, the strain contour distribution demonstrates clearly a change in the location of the region with high strain values, indicated with red colour, as the length of Δa is increased. For a small Δa of approximately 2 mm [Fig. 15(a)], the strain contour shows a red region that expands all over the bond-line thickness up to the adherend-adhesive interfaces, resulting in fracture onset close to one of the adherend-adhesive interfaces. However, for longer Δa's [Fig. 15(b) and (c)], the higher strains are concentrated around the pre-crack tip, leading to cohesive fracture onset. These results strongly support Δa as a length that determine the point of fracture onset.

In order to better show the strain contour evolution for increasing values of Δa, numerical simulations were ran. The load correspondent to fracture onset moment of a representative steel-steel adhesive joint with $\Delta a = 3.9$ mm was applied on FE models with varying Δa length from 0 up to 6 mm. The results are shown in Figs. 16 and 17, and were taken at the mid-width of the specimen ($B \pm 0$ mm). One should observe that the numerical and experimental strain contours should only be compared qualitatively. In fact, the FE model represents sharp bi-material corners and pre-crack tip unlike the experiments, in which finite radii exist at those regions.

For $\Delta a = 0$ mm, one can observe a singularity at the corners of the bond-line in Fig. 16(a). By increasing Δa from 2 up to 6 mm, one can observe a change in the location of the singularity, i.e. the higher values of the strain are found in the pre-crack tip region as shown in Figs. 16(b), 17(a) and (b). Moreover, an increase of Δa leads to larger unloaded areas, indicated by the dark blue colour in the cracked adhesive region. However, the corners do not need to be completely unloaded to have cohesive fracture onset, as shown in Fig. 17(a) where $\Delta a_{\text{exper.}}$ is considered and has resulted in cohesive fracture in the experimental tests. For cohesive fracture onset, the stress threshold must be first attained at the pre-crack tip region rather than at the bi-material corners.

From the proposed elastic-plastic model, two length scales are identified. The first one, l_p, in some cases can be interpreted as crack tip plastic radius, thus, solely associated with the material properties, including yield stress and critical fracture energy, of the adhesive material [10]. However, the process zone can further extend above the plastic radius depending on the second length scale. The second

Table 4
Dundurs parameters for different material combinations under plane-strain conditions.

Adherend/Adhesive	G_{adher} (MPa)	G_a (MPa)	ν_{adher} (–)	ν_a (–)	α (–)	β (–)
Steel/Epoxy	80769	752	0.300	0.33	0.98	0.25
GFRP/Epoxy	3897 [28]	752	0.252	0.33	0.65	0.15

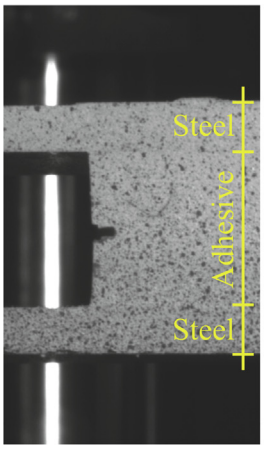

$\Delta a \approx 2.0$ mm
Close to interface
fracture onset

(a) Steel-steel bonded joint.

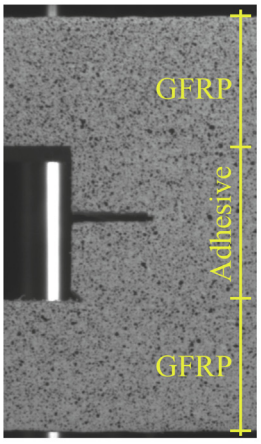

$\Delta a \approx 5.7$ mm
Cohesive fracture onset

(b) GFRP-GFRP bonded joint.

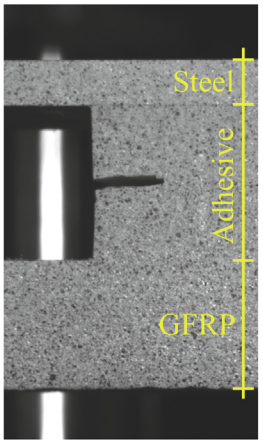

$\Delta a \approx 4.8$ mm
Cohesive fracture onset

(c) Steel-GFRP bonded joint.

Fig. 14. Examples of experimentally investigated Δa's.

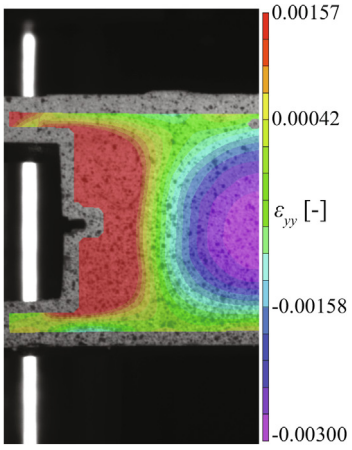

(a) Steel-steel bonded joint.

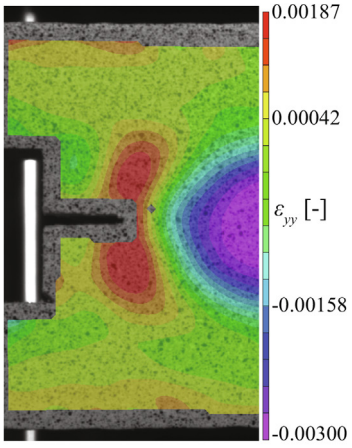

(b) GFRP-GFRP bonded joint.

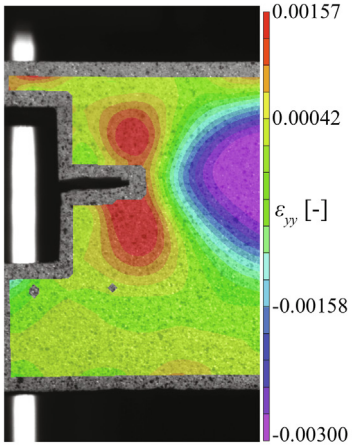

(c) Steel-GFRP bonded joint.

Fig. 15. Strain, ε_{yy}, contour at fracture onset moment for three different specimens.

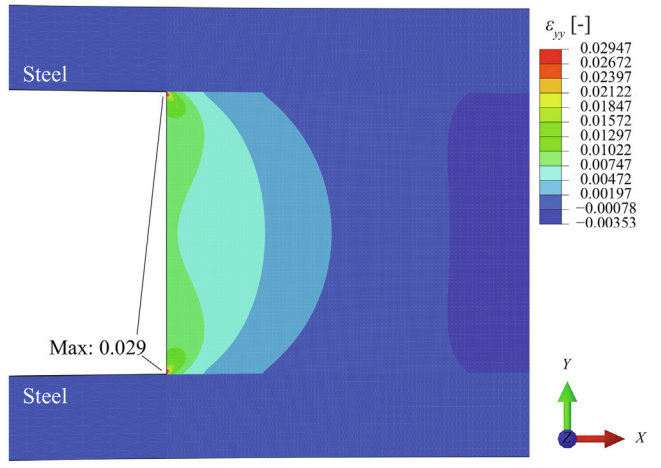

(a) Δa = 0 mm.

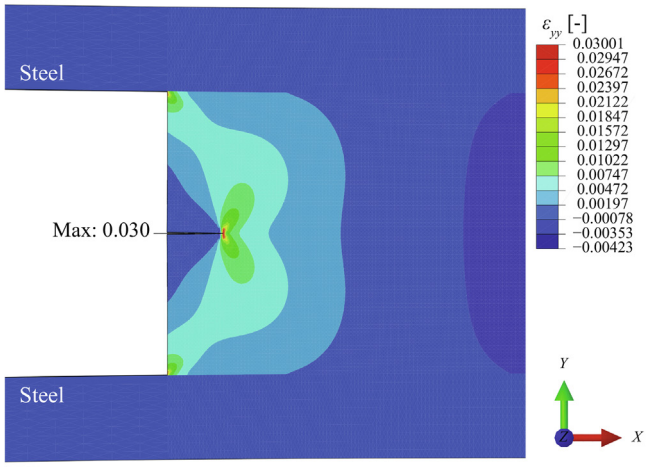

(b) Δa = 2 mm.

Fig. 16. Evolution of strain field, ε_{yy}, in steel-steel joint with increasing Δa. The results are taken along the mid-width of the model (B = 0 mm).

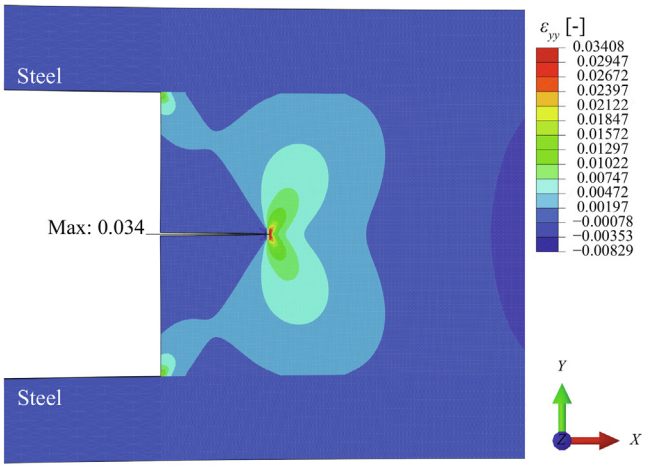

(a) $\Delta a_{exper.}$ = 3.9 mm.

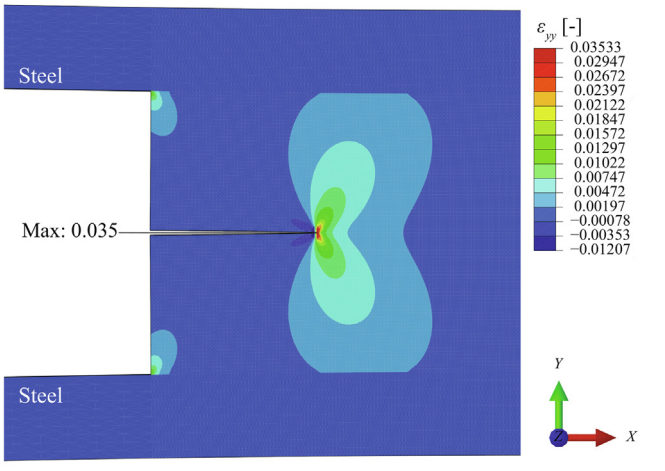

(b) Δa = 6 mm.

Fig. 17. *Continuation…* Evolution of strain field, ε_{yy}, in steel-steel joint with increasing Δa. The results are taken along the mid-width of the model (B = 0 mm).

characteristic dimension, associating distribution of the stress field along the joint with overall joint geometry and material properties, emerges as λ^{-1}. The parameter λ^{-1} is the characteristic length defined to solve the differential equation of a beam supported by an elastic medium. This parameter is function of the geometry and mechanical properties of the adhesive bond-line and adherends [15], as given by Eq. 11. Importantly, it is a parameter that is measurable and corresponds to the distance over which $\sigma_{yy} \geqslant 0$. We postulate existence of two non-dimensional parameters which can be used to craft an adhesive joint failure map:

- Case 1: $\frac{r_p}{t_a} > 1$ and $\Delta a = 0$ - the plastic regions builds up through the entire bond-line thickness and the joint will most likely fail in cohesive manner.
- Case 2: $\frac{r_p}{t_a} > 1$ and $\Delta a > 0$ - the joint will most likely fail in cohesive manner.
- Case 3: $\frac{r_p}{t_a} < 1$ and $\Delta a = 0$ - the joint will fail at or close the interface with the highest material mismatch.
- Case 4: $\frac{r_p}{t_a} < 1$ and $\Delta a > 0$ then another parameter needs to be taken into account - $\frac{\lambda^{-1}}{\Delta a}$. This parameter can be treated as a more general case of Griffith's diffusion line approach, which should enable capturing effects of bond-line confinement [39]. In specific, for the plate made from a single material $\lambda^{-1} \rightarrow \infty$ and the $\frac{\lambda^{-1}}{\Delta a} \rightarrow \infty$, implying that the stress is applied to the specimen remotely, i.e. $\sigma_{yy} = \sigma_{yy}^{\infty}$ and the original diffusion lines argument applies. In an adhesive joint, some transition Δa, defined as $\Delta a_{crit.}$, must exist at which the failure will change from interfacial (singular field at the corner/edge) to cohesive (singular stress field at the pre-crack tip), possibly resulting in diffusion lines as illustrated in Fig. 2.

All experiments carried out in this study correspond to case 4. An estimation of $2r_p \approx 1$ mm under plane-strain conditions is reported in a previous publication of the same authors, please see R.L. Fernandes et al. [32]. Therefore, $r_p < t_a$. Besides, in all joints was created a pre-crack at the mid-thickness of the adhesive bond-line during the manufacturing procedure, i.e. $\Delta a > 0$. From the experimental results, it was found out that, that regardless of the joint type, a ratio of $\frac{\lambda^{-1}}{\Delta a_{crit.}} \leqslant 2$ leads to cohesive fracture onset (i.e. at mid-adhesive thickness), considering both plane-strain and plane-stress conditions. Table 5 summarizes the experimental Δa's considered for all joint types as well as the ratio $\frac{\lambda^{-1}}{\Delta a}$ and corresponding failure type at fracture onset. The empirical relation for cohesive fracture onset can also be expressed as $(8E_a B/E_x^f I).(\Delta a_{crit.})^4 \geqslant 2t_a$, so that for a given material mismatch

Table 5
Empirical relation between λ^{-1} and Δa under plane-strain conditions.

Joint type	t_a (mm)	λ^{-1}_{steel} (mm)	λ^{-1}_{GFRP} (mm)	Δa (mm)	$\lambda^{-1}_{steel}/\Delta a$ (–)	$\lambda^{-1}_{GFRP}/\Delta a$ (–)	Fracture onset
Steel-steel	5.0	7.5	–	0.6	12.5	–	Close to interface
	5.0			2.0	3.9		Close to interface
	5.0			**3.9**	**1.9**		**Cohesive**
GFRP-GFRP	5.1	-	9.4	0.8	–	11.8	Close to interface
	5.0			**5.1**		**1.8**	**Cohesive**
	5.0			**5.7**		**1.6**	**Cohesive**
Steel-GFRP	5.0	7.5	9.4	0.5	15.1	18.9	Close to interface
	5.0			**4.8**	**1.5**	**1.9**	**Cohesive**
	5.0			**5.2**	**1.4**	**1.8**	**Cohesive**

$(\Delta a_{crit.}/h_{adher})^4 \sim (t_a/h_{adher})$ is the scaling relation for transition into cohesive fracture onset.

5.2. Crack path selection

The issue of crack path selection and stability depends upon local, crack tip loading and can be addressed in terms of the asymptotic stress field around the crack tip [40,41,37]. Let (r,θ) be polar coordinates centered at the crack tip of a crack in a homogeneous material. The stresses ahead of the crack tip ($\theta = 0$) are given by,

$$\begin{bmatrix} \sigma_{xx} & \sigma_{xy} \\ \sigma_{xy} & \sigma_{yy} \end{bmatrix} = \frac{K_I}{\sqrt{2\pi r}} \begin{bmatrix} 1 & 0 \\ 0 & 1 \end{bmatrix} + \frac{K_{II}}{\sqrt{2\pi r}} \begin{bmatrix} 0 & 1 \\ 1 & 0 \end{bmatrix} + \begin{bmatrix} T & 0 \\ 0 & 0 \end{bmatrix} + O(\sqrt{r}), \tag{27}$$

where K_I and K_{II} are the stress intensity factors of opening and shear modes, respectively, T is a stress acting parallel to the crack plane and $O(\sqrt{r})$ represents higher order terms. Please note that Eq. 27 is brought here to show how physically the T-stress term contributes to the stress field ahead of the crack tip. The T-stress is determined in sub-Section 5.2.1.

According to B. Cotterell and J.R. Rice [19], if a straight crack advancing in a homogeneous material with $K_{II} = 0$ is perturbed due to some micro-heterogeneity, a positive T-value drives the crack away from the straight trajectory while a negative T-value drives the crack back to initial trajectory. N. Fleck et al. [40] and B. Chen et al. [42,41,43] concluded that, similarly to the homogeneous materials, the magnitude of T-stress plays an important role in the directional stability of cracks in adhesive joints (stable cracks grow in a straight, non-wavy manner). The T-stress decreases with the thickness of the adhesive, resulting in higher probability of stable crack propagation if the thickness of the adhesive layer decreases. On the other hand, as the adherend thickness decreases, the T-stress increases due to the effect of adherend bending. Moreover, the T-stress also depends on the residual stress originating from joint manufacturing, due to the mismatch of the coefficients of thermal expansion and shrinkage.

Fig. 18 shows the representative crack growth paths in case of cohesive fracture onset for the adhesive joints investigated in this study. One of the features, observed by naked eye, of crack onset and growth in these joints is the deflection of the crack from the straight trajectory along the centre of the adhesive thickness. The adherends constraint effects in thick bond-lines are relieved to some extent and, thus, the adhesive bond-line is not entirely constrained. In the absence of stabilizing factor of compressive stresses (which are at a large distance from the crack tip, of order λ^{-1}, if compared to the asymptotic field), the crack is found to rapidly deflect out from the mid-adhesive thickness. Therefore, parameters such as the local crack tip loading, which may not be predominantly in mode I, and the T-stress control the unstable crack growth [40,41,43]. To better understand this behaviour, in the following sub-section, the T-stress at the crack tip is analysed for two different bond-line thicknesses considering steel-steel joints. Moreover, the overall shape of the crack path per joint configuration is discussed thereafter.

5.2.1. The role of T-stress

To quantify the T-stress in steel-steel DCB specimens with varying bond-line thickness (4 and 10 mm), finite element analysis was carried out. Both the adhesive and adherends were modelled as elastic materials (T-stress is calculated based on the load level and linear elastic material properties). The overall description of the 3D-models and material properties can be found in sub-Sections 3.2 and 2.1, respectively. As the T-stress depends on the residual stress in the adhesive, a thermal gradient representative of the cooling part of the curing cycle (from curing temperature, 80 °C, to laboratory temperature, 23 °C) was also included in the models. The coefficients of thermal expansion used in the models are listed in Table 6. The calculation of T-stress along the crack front is conducted within ABAQUS® program. Five contours were used in the analyses as a good independence of the T-stress distribution was obtained. Therefore, only the T-stress distributions taken from the outer contour (contour number 5) are shown.

Fig. 19 shows the results of the T-stress distributions along the crack tip for two different bond-line thicknesses: 4 and 10 mm. The first moment of crack growth visually identified during the experimental tests was picked as the loading case – points highlighted in Fig. 19 (a) and (b). As shown in Fig. 19(c), the T-stress increases with increasing bond-line thickness. These results are in agreement with the findings of B. Chen et al. [42]. Therefore, it seems that non-straight crack paths are more likely to occur in joints with a 10 mm thick adhesive bond-line than in joints with a bond-line of 4 mm. N.A. Fleck et al. [40] reported that the presence of mode II loading component and positive T-stress at the crack tip leads to crack kinking towards the interface.

5.2.2. Characteristic length of unstable propagation

Representative crack trajectories of each joint type investigated in this study are presented in Fig. 20. These trajectories can be analysed in terms of initial Δa length:

- In case of $\Delta a < \Delta a_{crit.}$, the fracture onset locus occurred close to one of the adhesive-adherend interfaces [Fig. 20(a)]. In the steel-GFRP joints, that interface was the adhesive-steel one. Afterwards, two different crack propagation behaviours were observed: i) asymmetric propagation along a remote plane from the mid-adhesive thickness – GFRP-GFRP and steel-GFRP joints, ii) alternating propagation within the bond-line, although closer to one interface than the other in some segments of the bonded area – steel-steel joints.
- In case of $\Delta a \geqslant \Delta a_{crit.}$, the fracture onset was cohesive, i.e. onset locus at mid-adhesive thickness [Fig. 20(b), (c) and (d)]. Afterwards, the direction of cracking was towards one of the adherends.

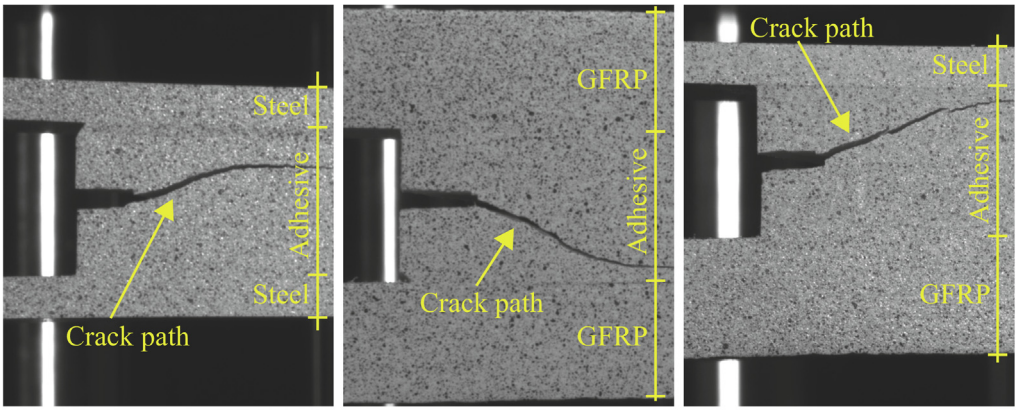

(a) Steel-steel joint. (b) GFRP-GFRP joint. (c) Steel-GFRP joint.

Fig. 18. Examples of crack growth paths in adhesive joints with 10 mm thick adhesive bond-line.

Table 6
Coefficients of thermal expansion (CTE).

Material	CTE ($\times 10^{-5}$ °C^{-1})	Reference
Steel	1.17	[44]
Araldite 2015	9.5	Supplier's technical data-sheet
GFRP	0.86 (longitudinal)	[44]
	2.21 (transverse)	[44]

In the steel-GFRP joints, the crack always steered away towards the steel adherend. The crack propagation occurred then along a remote plane from the adhesive centre-line up to the final failure.

According to B. Chen et al. [41,43], the energy available for the crack to grow decreases as the crack approaches an adhesive-adherend interface due to the rigid boundary of the adherend. As the adherends are tougher than the adhesive, the crack does not normally propagate into them. Instead, the crack follows the direction with the lowest critical fracture energy, being in the present study a straight path remote from the adhesive mid-thickness. N.A. Fleck et al. [40] found out that under remote mode I load, for some material combinations, there is an additional straight path, satisfying $K_{II} = 0$, off the adhesive centre-line, near one of the interfaces.

B. Chen et al. [41] numerically predicted the crack trajectories of directionally unstable cracks in DCB specimens for different values of adhesive thickness and different material systems characterized by

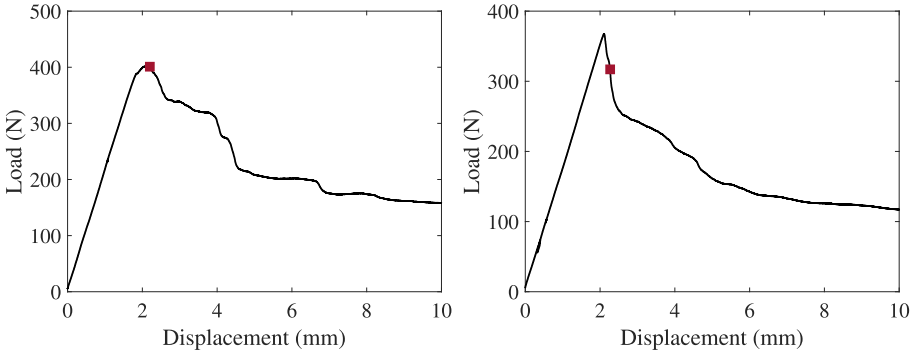

(a) $P-2\Delta$: $2t_a = 4$ mm, $a_{total} = 40.6$ mm [32]. (b) $P-2\Delta$: $2t_a = 10$ mm, $a_{total} = 43.1$ mm.

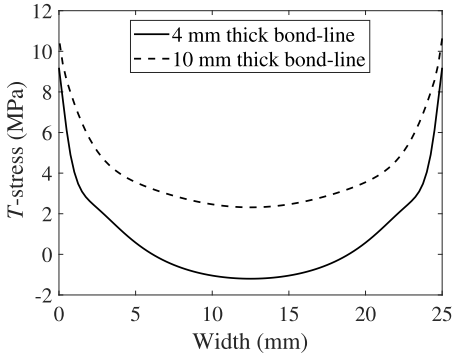

(c) T-stress distribution along the crack tip.

Fig. 19. Experimental load vs. displacement ($P-2\Delta$) curves and T-stress distribution at crack tip for DCB steel-steel specimens with different bond-line thicknesses.

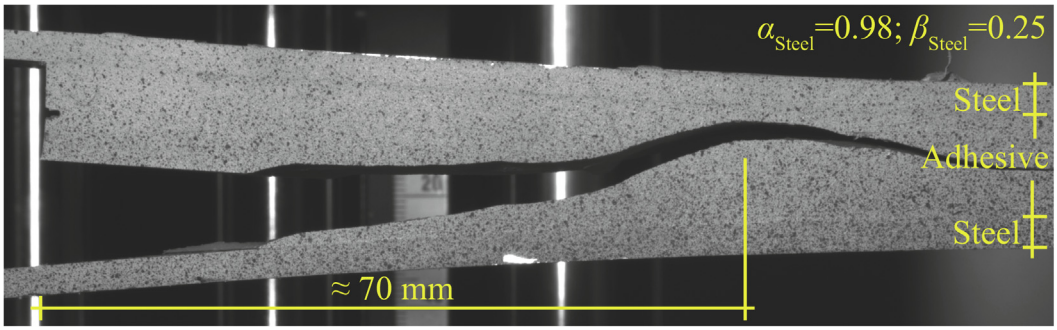

(a) Crack trajectory in steel-steel joint - near to adhesive-adherend interface fracture onset.

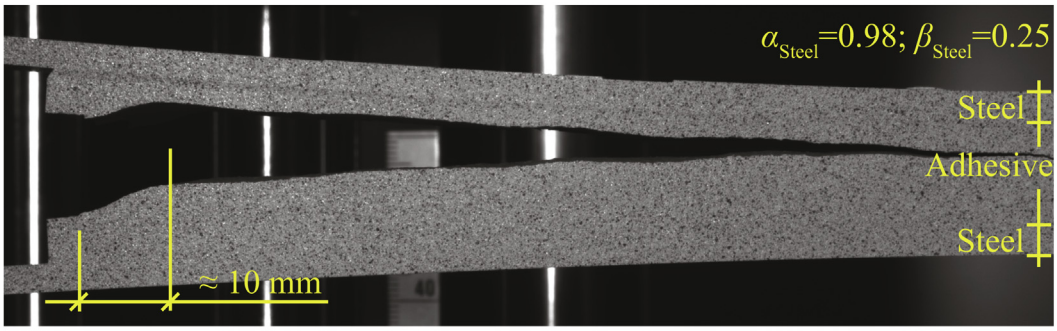

(b) Crack trajectory in steel-steel joint - cohesive fracture onset.

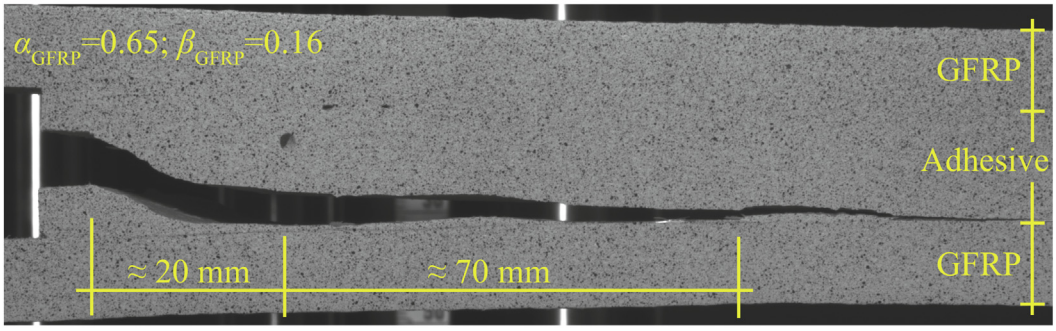

(c) Crack trajectory in GFRP-GFRP joint - cohesive fracture onset.

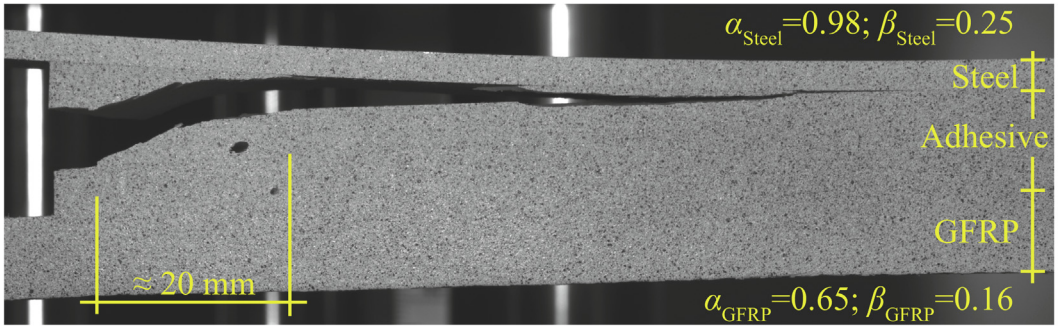

(d) Crack trajectory in steel-GFRP joint - cohesive fracture onset.

Fig. 20. Representative crack trajectories for different adhesive joints configurations with 10 mm thick bond-line.

Dundurs parameter α, Eq. 21. According to the authors, the crack trajectories for different material combinations are similar in shape, although the characteristic length, i.e. the horizontal distance in which the crack alternates its location from a region near to one adhesive-adherend interface to a region near to the opposite interface, decreases as the Dundurs parameter α increases. Both the critical local mixed-mode loading and the T-stress at the crack tip are found to occur at smaller crack lengths for higher material mismatch and, consequently, the characteristic length is predicted to be smaller.

In the present study, only the steel-steel joints with $\Delta a < \Delta a_{crit.}$ presented alternating crack propagation within the adhesive bond-line [Fig. 20(a)]. By comparing these crack trajectories with the predictions of B. Chen et al. [41], one can conclude that there is a qualitative agreement between both, but not a quantitative one. The numerically

predicted characteristic length (around 20–30 mm) is smaller than the experimental one (approximately 70 mm). These results may be explained by the fact that a load was applied horizontally to maintain a positive *T*-stress level in the numerical models, which might have resulted in higher values of *T*-stress and, thus, in more directionally unstable crack propagation (i.e. more wavy pattern) [40]. For the GFRP-GFRP and steel-GFRP, it seems that the critical loading conditions and stresses at crack tip did not reach the critical values, and the cracking direction along the remote plane off the adhesive centre-line was kept.

6. Concluding remarks

This study aimed in investigating the fracture onset and crack deflection in adhesive joints with thick bond-lines (≈10 mm) under global mode I loading. Single-material (i.e. steel-steel and GFRP-GFRP) and bi-material (i.e. steel-GFRP) double-cantilever beam joints bonded with a structural epoxy adhesive were tested. The joints were modelled analytically. To link the experimental findings to existing theoretical models, the behaviour of the different joints was also assessed numerically.

The Yamada's analytical model (based on the Euler-Bernoulli beam theory and on a beam supported by an elastic-plastic foundation for the free and the bonded regions of the adhesive joint, respectively) gives fairly good agreements with the experimental results, specially taking into account that no parameter fitting or adjustment was performed and the entire models rely on properties measured through either tensile or bending testing of constituents.

Both the initially linear part of the experimental load-displacement curves and the critical force at fracture onset were normalized by following the simple beam theory. These steps allow the comparison of the results here presented with the results of any other adhesive joints, regardless the materials and joint geometry.

The normalization of the critical force at fracture onset was made by considering joints with varying adhesive bond-line thickness (from 0.4 to 10 mm) and by distinguishing between cohesive and close to interface fracture onset (both failure types only happened for 10 mm thick bond-line). Similar values of the normalized critical force at fracture onset were found, regardless of the bond-line thickness. The difference between cohesive and close to interface fracture onset was less than 10% for the joints with a bond-line of 10 mm. This indicates that the adhesive was able to deform as a response to the external loading, even though in some cases the critical stress was first attained in a region close to one of the adherend-adhesive interfaces.

For thick adhesive bond-lines, such as 10 mm thick ones, geometric discontinuities, such as corners, and material discontinuities, such as adherend-adhesive interfaces, create local singularities where the threshold stress for fracture onset is attained first. To overcome this situation, a critical pre-crack length must be defined, $\Delta a_{\text{crit.}}$. The definition of $\Delta a_{\text{crit.}}$ follows the idealization of unloaded region near crack surfaces in an infinite homogeneous plate with a crack as postulated by A.A. Griffith;

For the case $r_p < t_a$ and $\Delta a > 0$, an empirical relation, in terms of geometrical and material properties of the joints, that defines the transition between non-cohesive (i.e. at or close an adherend-adhesive interface) and cohesive fracture onset was found - for a given material mismatch $(\Delta a_{\text{crit.}}/h_{\text{adher}})^4 \sim (t_a/h_{\text{adher}})$. In general, for $\Delta a < \Delta a_{\text{crit.}}$: the stress singularity near the bi-material corner rules over the stress singularity at the pre-crack tip. The bi-material corner with the highest modulus-mismatch, characterized by the highest Dundurs parameters, dictates the region of fracture initiation; for $\Delta a \geqslant \Delta a_{\text{crit.}}$: the stress singularity at the pre-crack tip is dominant, resulting in cohesive fracture onset.

In all joints with cohesive fracture onset, the cracking direction rapidly deflected out from the adhesive layer centre-line. Positive *T*-stress along the crack tip was numerically found considering 10 mm thick bond-line, being one of the factors for the unstable crack path. The crack propagation occurred then along a remote plane from the adhesive centre-line up to the final failure.

Declaration of Competing Interest

The authors declare that they have no known competing financial interests or personal relationships that could have appeared to influence the work reported in this paper.

Acknowledgements

This research was carried out under project number S32.6.14552a – Durabond in the framework of the Partnership Program of the Materials innovation institute M2i (www.m2i.nl) and the Technology Foundation TTW (www.stw.nl), which is part of the Netherlands Organization for Scientific Research (www.nwo.nl). The Durabond project is linked to a Joint Industry Project (JIP) set up by TNO, separately funded by *Topconsortium voor Kennis en Innovatie (TKI) HighTech Systemen* & *Materialen (HTSM)*. This work was also supported with a short term scientific mission (STSM), which was developed under the COST Action CA18120 (CERTBOND) and supported by COST (European Cooperation in Science and Technology).

Appendix A

Ten unknown coefficients and the plastic zone size are obtained by satisfying boundary conditions at $x = l_e$,

$$\frac{d^3 w_3}{dx^3} = 0, \tag{28}$$

$$\frac{d^2 w_3}{dx^2} = 0, \tag{29}$$

and continuity conditions at $x = -l_p$,

$$w_1 = w_2, \tag{30}$$

$$\frac{dw_1}{dx} = \frac{dw_2}{dx}, \tag{31}$$

$$\frac{d^2 w_1}{dx^2} = \frac{d^2 w_2}{dx^2}, \tag{32}$$

$$\frac{d^3 w_1}{dx^3} = \frac{d^3 w_2}{dx^3}, \tag{33}$$

and at $x = 0$,

$$w_2 = w_3, \tag{34}$$

$$\frac{dw_2}{dx} = \frac{dw_3}{dx}, \tag{35}$$

$$\frac{d^2 w_2}{dx^2} = \frac{d^2 w_3}{dx^2}, \tag{36}$$

$$\frac{d^3 w_2}{dx^3} = \frac{d^3 w_3}{dx^3}, \tag{37}$$

$$\frac{d^4 w_2}{dx^4} = \frac{d^4 w_3}{dx^4}. \tag{38}$$

The mathematical details of the solution procedure appear in [16]. The results for the case where the bonded region is sufficiently long are,

$$\gamma_1 = \frac{P\lambda}{\sigma_y B}, \tag{39}$$

$$\gamma_2 = \frac{(l_f - l_p)P\lambda^2}{\sigma_y B}, \tag{40}$$

$$\gamma_3 = \frac{\sigma_y B}{E_x^t I\lambda^3}, \tag{41}$$

$$\lambda l_p = \gamma_1 - 1 + \sqrt{\gamma_1^2 + 2\gamma_2}, \tag{42}$$

$$C_1 = \gamma_3\lambda^2(\gamma_1 - \lambda l_p), \tag{43}$$

$$C_2 = \gamma_3\lambda\left(\gamma_2 - \frac{1}{2}\lambda^2 l_p^2 + \gamma_1\lambda l_p\right), \tag{44}$$

$$C_3 = (K_2 + K_4)\lambda, \tag{45}$$

$$C_4 = K_1, \tag{46}$$

$$K_1 = \frac{\sigma_y B}{4E_x^t I\lambda^4}, \tag{47}$$

$$K_2 = -K_1, \tag{48}$$

$$K_3 = \frac{C_2}{2\lambda^2}, \tag{49}$$

$$K_4 = -K_3, \tag{50}$$

$$R_1 = \frac{\gamma_3}{6}(\lambda l_p)^3 + C_3, \tag{51}$$

$$R_2 = \frac{\gamma_3}{24\lambda}[(\lambda l_p)^4 + 6]. \tag{52}$$

When l_p is not positive, the plastic zone does not exist. Though Eq. 47 is no longer valid, the set of equations Eqs. (39)–(41), (43), (44), (48), (49) and (50) can still be solved by setting $l_p = 0$ and eliminating Eq. 38,

$$C_1 = \frac{P}{E_x^t I}, \tag{53}$$

$$C_2 = \frac{(l_f - l_p)P}{E_x^t I}, \tag{54}$$

$$K_1 = \frac{P}{2E_x^t I\lambda^3} + \frac{(l_f - l_p)P}{2E_x^t I\lambda^2}, \tag{55}$$

$$K_2 = -K_1, \tag{56}$$

$$K_4 = -K_3, \tag{57}$$

$$R_1 = -(K_1 - K_4)\lambda, \tag{58}$$

$$R_2 = K_1. \tag{59}$$

Appendix B. Data DOI

The data required to reproduce these findings are available at: https://doi.org/10.4121/13148441.

References

[1] Saeedifar M, Saleh MN, Freitas ST, Zarouchas D. Damage characterization of adhesively-bonded bi-material joints using acoustic emission. Compos Part B 176 (107356).https://doi.org/10.1016/j.compositesb.2019.107356..

[2] Freitas ST, Kolstein H, Bijlaard F. Lightweight reinforcement systems for fatigue-cracked orthotropic bridge decks. Struct Eng Int: J Int Assoc Bridge Struct Eng 2013;23:458–67. https://doi.org/10.2749/101686613X13627347100356.

[3] International Association of Classification Societies. No. 47 Shipbuilding and Repair Quality Standard (Rev. 7 June 2013), Tech. Rep. 1996 (2013)..

[4] Mishnaevsky L, Branner K, Petersen HN, Beauson J, McGugan M, Sørensen BF. Materials for wind turbine blades: an overview. Materials 2017;10:1285. https://doi.org/10.3390/ma10111285.

[5] Bogy DB. On the problem of edge-bonded elastic quarter-planes loaded at the boundary. Int J Solids Struct 1970;6:1287–313. https://doi.org/10.1016/0020-7683(70)90104-6.

[6] Hutchinson JW, Mear ME, Rice JR. Crack paralleling an interface between dissimilar materials. J Appl Mech 1987;54:828–32. https://doi.org/10.1115/1.3173124.

[7] Suo Z, Hutchinson JW. Sandwich test specimens for measuring interface crack toughness. Mater Sci Eng: A 1989;107:135–43. https://doi.org/10.1016/0921-5093(89)90382-1.

[8] Reedy ED, Guess TR. Interface corner failure analysis of joint strength: effect of adherend stiffness. Int J Fracture 1997;88:305–14. https://doi.org/10.1023/A:1007436110715.

[9] Akisanya AR, Meng CS. Initiation of fracture at the interface corner of bi-material joints. J Mech Phys Solids 2003;51:27–46. https://doi.org/10.1016/S0022-5096(02)00076-5.

[10] Perez N. Fracture mechanics. Springer; 2017.https://doi.org/10.1007/b118073..

[11] Depinoy S, Strepenne F, Massart TJ, Godet S, Pardoen T. Interface toughening in multilayered systems through compliant dissipative interlayers. J Mech Phys Solids 2019;130:1–20. https://doi.org/10.1016/j.jmps.2019.05.013.

[12] Benbow JJ, Roesler FC. Experiments on controlled fractures. Proc Phys Soc B 1957;70:201–11. https://doi.org/10.1088/0370-1301/70/2/307.

[13] Kanninen MF. An augmented double cantilever beam model for studying crack propagation and arrest. Int J Fracture 1973;9:83–92.

[14] Van Loock F, Thouless MD, Fleck NA. Tensile fracture of an adhesive joint: the role of crack length and of material mismatch. J Mech Phys Solids 2019;130:330–48. https://doi.org/10.1016/j.jmps.2019.06.004.

[15] Penado FE. A closed form solution for the energy release rate of the double cantilever beam specimen with an adhesive layer. J Compos Mater 1993;27:383–407. https://doi.org/10.1177/002199839302700403.

[16] Yamada SE. Elastic/plastic fracture analysis for bonded joints. Eng Fracture Mech 1987;27:315–28. https://doi.org/10.1016/0013-7944(87)90149-4.

[17] Dundurs J. Effect of elastic constants on stress in a composite under plane deformation. J Compos Mater 1967;1:310–22. https://doi.org/10.1177/002199836700100306.

[18] Bogy DB. Two edge-bonded elastic wedges of different materials and wedge angles under surface tractions. J Appl Mech 1971;38:377–86. https://doi.org/10.1115/1.3408786.

[19] Cotterell B, Rice JRF. Slightly curved or kinked cracks. Int J Fracture 1980;16:155–69. https://doi.org/10.1007/BF00012619.

[20] Suo Z, Hutchinson JW. Interface crack between two elastic layers. Int J Fracture 1990;43:1–18. https://doi.org/10.1007/BF00018123.

[21] Hutchinson JW, Suo Z. Mixed mode cracking in layered materials. In Advances in applied mechanics. vol. 29, Elsevier; 1991. pp. 63–191.https://doi.org/10.1016/S0065-2156(08)70164-9..

[22] Wang CH. Analysis of cracks in constrained layers. Int J Fracture 1997;83:1–7. https://doi.org/10.1023/A:1007313620138.

[23] ASTM D 5528/ D 5528–13. Standard Test Method for Mode I Interlaminar Fracture Toughness of Unidirectional Fiber-Reinforced Polymer Matrix Composites; 2013..

[24] Blackman BRK, Kinloch AJ, Paraschi M. The determination of the mode ii adhesive fracture resistance, G_{IIC}, of structural adhesive joints: an effective crack length approach. Eng Fracture Mech 2005;72:877–97. https://doi.org/10.1016/j.engfracmech.2004.08.007.

[25] Bazant ZP, Cedolin L. Stability of structures: elastic, inelastic, fracture and damage theories. World Scientific; 2010.

[26] ISO 527:2012. Plastics – determination of tensile properties; 2012..

[27] Wang W, Lopes Fernandes R, Teixeira de Freitas S, Zarouchas D, Benedictus R. How pure mode I can be obtained in bi-material bonded DCB joints: a longitudinal strain-based criterion. Compos Part B: Eng 2018;153:137–48. https://doi.org/10.1016/j.compositesb.2018.07.033.

[28] Lopes Fernandes R, Teixeira de Freitas S, Budzik MK, Poulis JA, Benedictus R. Role of adherend material on the fracture of bi-material composite bonded joints. Compos Struct 252 (112643).https://doi.org/10.1016/j.compstruct.2020.112643..

[29] Li G, Wang X, Li A, Wang W, Zheng L. Fabrication and adhesive properties of thin organosilane films coated on low carbon steel substrates. Surf Coat Technol 2007;201:9571–8. https://doi.org/10.1016/j.surfcoat.2007.04.032.

[30] Chow CL, Woo CW, Sykes JL. On the determination and application of cod to epoxy-bonded aluminium joints. J Strain Anal 1979;14:37–42. https://doi.org/10.1243/03093247V142037.

[31] Jumel J, Budzik MK, Shanahan MER. Beam on elastic foundation with anticlastic curvature: application to analysis of mode I fracture tests. Eng Fracture Mech 2011;78:3253–69. https://doi.org/10.1016/j.engfracmech.2011.09.014.

[32] Lopes Fernandes R, Teixeira de Freitas S, Budzik MK, Poulis JA, Benedictus R. From thin to extra-thick adhesive layer thicknesses: fracture of bonded joints under mode I loading conditions. Eng Fracture Mech 218 (106607).https://doi.org/10.1016/j.engfracmech.2019.106607..

[33] Davidson BD, Schapery RA. Effect of finite width on deflection and energy release rate of an orthotropic double cantilever specimen. J Compos Mater 1988;22:640–56. https://doi.org/10.1177/002199838802200704.
[34] Møberg A, Budzik MK, Jensen HM. Crack front morphology near the free edges in double and single cantilever beam fracture experiments. Eng Fracture Mech 2017;175:219–34. https://doi.org/10.1016/j.engfracmech.2017.01.030.
[35] Budzik MK, Heide-Jørgensen S. Branching and softening of loading path during onset of crack at elastic-brittle interface. Mech Mater 2018;127:1–13. https://doi.org/10.1016/j.mechmat.2018.08.013.
[36] Bogy DB. Edge-bonded dissimilar orthogonal elastic wedges under normal and shear loading. J Appl Mech 1968;35:460–6. https://doi.org/10.1115/1.3601236.
[37] Budzik MK, Jumel J, Shanahan MER. 4-Point beam tensile test on a soft adhesive. Mater Design 2013;46:134–41. https://doi.org/10.1016/j.matdes.2012.10.011.
[38] Dundurs J. Discussion: “edge-bonded dissimilar orthogonal elastic wedges under normal and shear loading” (Bogy, D.B., 1968, ASME J. Appl. Mech., 35, pp. 460–466). J Appl Mech 36; 1969: 650–652.https://doi.org/10.1115/1.3564739..
[39] Pardoen T, Ferracin T, Landis CM, Delannay F. Constraint effects in adhesive joint fracture. J Mech Phys Solids 2005;53(9):1951–83. https://doi.org/10.1016/j.jmps.2005.04.009.
[40] Fleck NA, Hutchinson JW, Suo Z. Crack path selection in a brittle adhesive layer. Int J Solids Struct 1991;27:1683–703. https://doi.org/10.1016/0020-7683(91)90069-R.
[41] Chen B, Dillard DA. Numerical analysis of directionally unstable crack propagation in adhesively bonded joints. Int J Solids Struct 2001;38:6907–24. https://doi.org/10.1016/S0020-7683(01)00006-3.
[42] Chen B, Dillard DA. The effect of the T-stress on crack path selection in adhesively bonded joints. Int J Adhesion Adhesives 2001;21:357–68. https://doi.org/10.1016/S0143-7496(01)00011-2.
[43] Chen B, Dillard DA, Dillard JG, Clark Jr RL. Crack path selection in adhesively-bonded joints: the role of material properties. J Adhesion 2001;75:405–34. https://doi.org/10.1080/00218460108029613.
[44] Kaw AK. Mechanics of Composite Materials. 2nd ed. CRC Press; 2006.